INTERNATIONAL JOURNAL FOR NUMERICAL METHODS IN FLUIDS, VOL. 15, 1073–1118 (1992)

A FINITE ELEMENT STUDY OF INCOMPRESSIBLE FLOWS PAST OSCILLATING CYLINDERS AND AEROFOILS

S. MITTAL AND T. E. TEZDUYAR

Department of Aerospace Engineering and Mechanics, Army High-Performance Computing Research Center, and Minnesota Supercomputer Institute, University of Minnesota, 1200 Washington Avenue South, Minneapolis, MN 55415, U.S.A.

SUMMARY

We present our numerical results for certain unsteady flows past oscillating cylinders and aerofoils. The computations are based on the stabilized space–time finite element formulation. The implicit equation systems resulting from the space–time finite element discretizations are solved using iterative solution techniques.

One of the problems studied is flow past a cylinder which is forced to oscillate in the horizontal direction. In this case we observe a change from an unsymmetric mode of vortex shedding to a symmetric one. An extensive study was carried out for the case in which a cylinder is mounted on lightly damped springs and allowed to oscillate in the vertical direction. In this case the motion of the cylinder needs to be determined as part of the solution, and under certain conditions this motion changes the vortex-shedding pattern of the flow field significantly. This non-linear fluid–structure interaction exhibits certain interesting behaviour such as 'lock-in' and 'hysteresis', which are in good agreement with the laboratory experiments carried out by other researchers in the past. Preliminary results for flow past a pitching aerofoil are also presented.

KEY WORDS Space–time Finite elements Incompressible flows Galerkin/least-squares Deforming spatial domain Oscillating cylinder Pitching aerofoil Clustered element-by-element GMRES Vortex shedding Vortex-induced oscillations Lock-in Hysteresis

1. INTRODUCTION

Recently, Tezduyar *et al.*[1,2] introduced the DSD/ST (deforming spatial domain/space–time) procedure and applied it to several unsteady incompressible flow problems involving moving boundaries and interfaces, such as free surface flows, liquid drops, two-liquid flows and flows with drifting cylinders. In this paper we use the same method to study certain unsteady flow problems involving oscillating cylinders and aerofoils. The DSD/ST method is based on the space–time formulation with the GLS (Galerkin/least-squares) stabilization. More information on the space–time finite element formulation with the GLS stabilization for problems with fixed spatial domains can be found in References 3–6. Because the space–time formulation involves finite element discretization not only in space but also in time, the deformation of the spatial domain is taken into account automatically. In the DSD/ST procedure the frequency of remeshing is minimized. Here we define remeshing as the process of generating a new mesh and projecting the solution from the old mesh to the new one. Since remeshing generally involves projection errors, minimizing the frequency of remeshing results in minimizing the projection errors. Minimizing the frequency of remeshing also results in an increase in the parallelization potential of the

0271–2091/92/211073–46$28.00 *Received March 1992*

computations. For all results presented in this paper, computations were performed using mesh-moving schemes that eliminate the need for remeshing.

To reduce the computational cost associated with solving the implicit equation systems resulting from the space–time finite element discretizations, efficient iterative solution techniques need to be employed. Here we use the generalized minimal residual (GMRES)[7] iteration algorithm in conjunction with the clustered element-by-element (CEBE)[8] preconditioners.

The first case studied is flow past a horizontally oscillating cylinder at Reynolds number 100. This leads to a symmetric mode of vortex shedding even though the computations start with an unsymmetric, temporally periodic solution obtained for flow past a fixed cylinder at Reynolds number 100. The second case studied involves flow past a cylinder that is mounted on flexible supports and is free to respond to fluid forces in the vertical direction. Consequently, the motion of the cylinder itself needs to be determined as part of the solution. The Reynolds number for this study varies between 290 and 360. This problem represents a case of vortex-induced oscillations and the aim of this study is to have an in-depth understanding of this non-linear fluid–structure interaction phenomenon when the vortex-shedding frequency is close to the natural frequency of the oscillator. Over a limited range the motion of the cylinder controls its vortex-shedding frequency; this phenomenon is called 'lock-in'.[9–16] This effect also manifests itself in shaping the structure of the wake downstream of the cylinder. Compared to the wake of a fixed cylinder, the longitudinal spacing between the vortices in the wake of an oscillating cylinder increases or decreases depending on whether the cylinder vibration frequency is smaller or larger than the vortex-shedding frequency for a fixed cylinder.[12] For certain Reynolds numbers, depending on the initial oscillation amplitude, the oscillator reaches two different temporally periodic vibration amplitudes. This phenomenon can also be interpreted as a 'hysteresis'-type behaviour, since the solution depends on whether the Reynolds number being considered is approached from the lower or the higher side.[10] We attempt to explain the cause of this double-amplitude behaviour by carrying out a linear oscillator analysis and viewing the resulting cylinder response along with certain experimental data reported by Blevins.[9] These experimental data for flow past a vertically oscillating cylinder relate the cylinder oscillation amplitude needed for the shedding frequency to 'lock in' to its vibration frequency. Recently, other researchers[17, 18] have also been involved in the investigation of the fluid–structure interaction phenomenon using finite element techniques. The last case we study is flow past a NACA 0012 aerofoil forced to pitch about its half-chord point at Reynolds number 1000. These preliminary computations were performed using a new mesh-moving scheme that we designed to handle the motion of any object without the need for remeshing. The mesh-moving scheme used for the oscillating cylinders is a special case of this more general scheme. The flow patterns obtained from these preliminary computations compare qualitatively well with similar experimental and numerical results reported by other researchers.[19, 20] We plan to extend this study to investigate the phenomenon of dynamic stall which might occur during a severe manoeuvre of a fighter aircraft.

2. THE GOVERNING EQUATIONS

Let $\Omega_t \in \mathbb{R}^{n_{sd}}$ be the spatial domain at time $t \in (0, T)$, where n_{sd} is the number of space dimensions. Let Γ_t denote the boundary of Ω_t. We consider the following velocity–pressure formulation of the Navier–Stokes equations governing unsteady incompressible flows:

$$\rho\left(\frac{\partial \mathbf{u}}{\partial t} + \mathbf{u} \cdot \nabla \mathbf{u}\right) - \nabla \cdot \sigma = \mathbf{0} \quad \text{on } \Omega_t \; \forall t \in (0, T), \tag{1}$$

$$\nabla \cdot \mathbf{u} = 0 \quad \text{on } \Omega_t \; \forall t \in (0, T), \tag{2}$$

where ρ and $\mathbf{u}$ are the density and the velocity respectively and σ is the stress tensor given as

$$\sigma(p, \mathbf{u}) = -p\mathbf{I} + 2\mu\varepsilon(\mathbf{u}), \tag{3}$$

with

$$\varepsilon(\mathbf{u}) = \tfrac{1}{2}[\nabla\mathbf{u} + (\nabla\mathbf{u})^{\mathrm{T}}]. \tag{4}$$

Here p and μ are the pressure and the dynamic viscosity respectively and $\mathbf{I}$ is the identity tensor. The part of the boundary at which the velocity is assumed to be specified is denoted by $(\Gamma_t)_g$:

$$\mathbf{u} = \boldsymbol{g} \quad \text{on } (\Gamma_t)_g \, \forall\, t \in (0, T). \tag{5}$$

The 'natural' boundary conditions associated with (1) are the conditions on the stress components, and these are the conditions assumed to be imposed at the remaining part of the boundary:

$$\mathbf{n} \cdot \sigma = \boldsymbol{h} \quad \text{on } (\Gamma_t)_h \, \forall\, t \in (0, T). \tag{6}$$

The homogeneous version of (6), which corresponds to the 'traction-free' (i.e. zero normal and shear stress) conditions, is often imposed at the outflow boundaries. As initial condition, a divergence-free velocity field $\mathbf{u}_0(\mathbf{x})$ is specified over the domain Ω_t at $t = 0$:

$$\mathbf{u}(\mathbf{x}, 0) = \mathbf{u}_0(\mathbf{x}) \quad \text{on } \Omega_0. \tag{7}$$

3. THE STABILIZED SPACE–TIME FINITE ELEMENT FORMULATION

In the space–time finite element formulation the time interval $(0, T)$ is partitioned into subintervals $I_n = (t_n, t_{n+1})$, where t_n and t_{n+1} belong to an ordered series of time levels $0 = t_0 < t_1 < \ldots < t_N = T$. It was first shown by Tezduyar *et al.*[1, 2] that the stabilized space–time finite element formulation can be effectively applied to fluid dynamics computations involving moving boundaries and interfaces. In this formulation the spatial domains at various time levels are allowed to vary. We let $\Omega_n = \Omega_{t_n}$ and $\Gamma_n = \Gamma_{t_n}$, and define the space–time slab Q_n as the space–time domain enclosed by the surfaces Ω_n, Ω_{n+1} and P_n. Here P_n, the lateral surface of Q_n, is the surface described by the boundary Γ as t traverses I_n. Similarly to the way it was represented by equations (5) and (6), P_n is decomposed into $(P_n)_g$ and $(P_n)_h$ with respect to the type of boundary condition being imposed.

Finite element discretization of a space–time slab Q_n is achieved by dividing it into elements Q_n^e, $e = 1, 2, \ldots, (n_{el})_n$, where $(n_{el})_n$ is the number of elements in the space–time slab Q_n. Associated with this discretization, for each space–time slab we define the following finite element interpolation function spaces for the velocity and pressure:

$$(S_{\mathbf{u}}^h)_n = \{\mathbf{u}^h \mid \mathbf{u}^h \in [H^{1h}(Q_n)]^{n_{sd}},\ \mathbf{u}^h \doteq \boldsymbol{g}^h \text{ on } (P_n)_g\}, \tag{8}$$

$$(V_{\mathbf{u}}^h)_n = \{\mathbf{w}^h \mid \mathbf{w}^h \in [H^{1h}(Q_n)]^{n_{sd}},\ \mathbf{w}^h \doteq \mathbf{0} \text{ on } (P_n)_g\}, \tag{9}$$

$$(S_p^h)_n = (V_p^h)_n = \{q^h \mid q^h \in H^{1h}(Q_n)\}. \tag{10}$$

Here $H^{1h}(Q_n)$ represents the finite-dimensional function space over the space–time slab Q_n. This space is formed by using, over the parent (element) domain, first-order polynomials in space and time. It is also possible to use zeroth-order polynomials in time. In either case, globally, the interpolation functions are continuous in space but discontinuous in time.

The space–time formulation of (1)–(7) can be written as follows: start with

$$(\mathbf{u}^h)_0^- = (\mathbf{u}_0)^h; \tag{11}$$

sequentially for $Q_1, Q_2, \ldots, Q_{N-1}$, given $(\mathbf{u}^h)_n^-$, find $\mathbf{u}^h \in (S_u^h)_n$ and $p^h \in (S_p^h)_n$ such that $\forall \mathbf{w}^h \in (V_u^h)_n$ and $\forall q^h \in (V_p^h)_n$

$$\int_{Q_n} \mathbf{w}^h \cdot \rho\left(\frac{\partial \mathbf{u}^h}{\partial t} + \mathbf{u}^h \cdot \nabla \mathbf{u}^h\right) dQ + \int_{Q_n} \varepsilon(\mathbf{w}^h) : \sigma(p^h, \mathbf{u}^h)\, dQ$$

$$- \int_{(P_n)_h} \mathbf{w}^h \cdot \boldsymbol{h}\, dP + \int_{Q_n} q^h \rho \nabla \cdot \mathbf{u}^h\, dQ + \int_{\Omega} (\mathbf{w}^h)_n^+ \cdot \rho[(\mathbf{u}^h)_n^+ - (\mathbf{u}^h)_n^-]\, d\Omega$$

$$+ \sum_{e=1}^{(n_{el})_n} \int_{Q_n^e} \tau\left[\rho\left(\frac{\partial \mathbf{w}^h}{\partial t} + \mathbf{u}^h \cdot \nabla \mathbf{w}^h\right) - \nabla \cdot \sigma(q^h, \mathbf{w}^h)\right] \cdot \left[\rho\left(\frac{\partial \mathbf{u}^h}{\partial t} + \mathbf{u}^h \cdot \nabla \mathbf{u}^h\right) - \nabla \cdot \sigma(p^h, \mathbf{u}^h)\right] dQ$$

$$+ \sum_{e=1}^{(n_{el})_n} \int_{Q_n^e} \delta \nabla \cdot \mathbf{w}^h \rho \nabla \cdot \mathbf{u}^h\, dQ = 0. \tag{12}$$

In the variational formulation given by (12) the following notation is being used:

$$(\mathbf{u}^h)_n^{\pm} = \lim_{\delta \to 0} \mathbf{u}^h(t_n \pm \delta), \tag{13}$$

$$\int_{Q_n} (\ldots)\, dQ = \int_{I_n} \int_{\Omega} (\ldots)\, d\Omega\, dt, \tag{14}$$

$$\int_{P_n} (\ldots)\, dP = \int_{I_n} \int_{\Gamma} (\ldots)\, d\Gamma\, dt. \tag{15}$$

Remarks

1. In equation (12) the series of integrals involving the coefficients τ and δ are the least-squares terms added to the Galerkin variational formulation to assure the numerical stability of the computations. This kind of stabilization of the Galerkin formulation is referred to as the Galerkin/least-squares (GLS) procedure and can be considered as a generalization of the stabilization based on the streamline upwind/Petrov–Galerkin (SUPG) and pressure-stabilizing/Petrov–Galerkin (PSPG) procedures employed for incompressible flows.[21] It is with such stabilization procedures that it is possible to use elements which have equal-order interpolation functions for velocity and pressure and which are otherwise unstable. The coefficient τ is defined as

$$\tau = \left[\left(\frac{2\|\mathbf{u}^h\|}{h}\right)^2 + \left(\frac{4\nu}{h^2}\right)^2\right]^{-1/2}, \tag{16}$$

where h is the element length. In this paper, for all problems involving cylinders, we use $\delta = 0$. For the problem involving an oscillating aerofoil the expression for δ is the same as the one used by Franca and Frey,[22] i.e.

$$\delta = \frac{h}{2}\|\mathbf{u}^h\| z, \tag{17}$$

where z is defined as

$$\frac{z}{2} = \begin{cases} \frac{1}{3}Re_u/2, & Re_u/2 \leqslant 3, \\ 1, & Re_u/2 \geqslant 3. \end{cases} \tag{18}$$

Here Re_u is the element Reynolds number defined as

$$Re_u = \frac{\| \mathbf{u}^h \| h}{2\nu}. \tag{19}$$

This form of z is very similar to the one used by Tezduyar *et al.*[21]

2. Because the finite element interpolation functions are discontinuous in time, the fully discrete equations can be solved one space–time slab at a time. Still, the memory needed for the global matrices involved in this method is quite substantial. However, iteration methods can be employed to substantially reduce the cost involved in solving the linear equation systems arising from the space–time finite element discretization. It was shown by Liou and Tezduyar[8] that the clustered element-by-element (CEBE) preconditioners together with the generalized minimal residual (GMRES) method[7] can be effectively used to reduce the associated cost significantly. All results reported here were computed by using such techniques.
3. With the DSD/ST procedure, to facilitate the motion of solid boundaries, we need to move the boundary nodes with the velocity of the fluid at those nodes. Except for this restriction we have the freedom to move all the nodes any way we would like to. With this freedom we can move the mesh in such a way that we only need to remesh when it becomes necessary to do so to prevent unacceptable degrees of mesh distortion and potential entanglements. By minimizing the frequency of remeshing, we minimize the projection errors expected to be introduced by remeshing. Furthermore, by minimizing the frequency of remeshing, we increase the parallelization potential of the computations and this is a desirable feature especially for massively parallel computations. For the problems involving oscillating cylinders we use the mesh-moving scheme described by Tezduyar *et al.*[2] In this paper we introduce a more general mesh-moving scheme for flows involving moving objects. Preliminary results are presented for a pitching aerofoil using the same scheme.

4. NUMERICAL RESULTS AND DISCUSSION

All solutions presented here were obtained with interpolation functions that are spatially bilinear and temporally linear. Nodal values of the vorticity and streamfunction were obtained by least-squares interpolation.

4.1. Unsteady flows past a circular cylinder

In all cases involving a circular cylinder the computational values for the cylinder radius and the freestream velocity are 1·0 and 0·125 respectively and the time step size is 1·0. The Reynolds number is based on the freestream velocity and the cylinder diameter. The dimensions of the computational domain, normalized by the cylinder radius, are 61·0 and 32·0 in the flow and cross-flow directions respectively. The zero-displacement location for the cylinder is at (16, 16) relative to the lower left corner of the domain. The mesh employed consists of 4060 elements and 4209 nodes. Symmetry conditions are imposed at the upper and lower computational boundaries and the traction-free condition is imposed at the outflow boundary. The periodic solution for flow past a fixed cylinder is obtained by introducing a short-term perturbation to the symmetric solution. In all our computations, to solve the implicit equation systems resulting from the space–time finite element discretization, we use the GMRES iteration method with the CEBE preconditioners. At every time step approximately 25 000 equations are solved simultaneously. We chose a Krylov vector space of dimension 25 and an average cluster size of 23 elements. For

this set of problems, compared to the direct solution method, the CEBE technique takes less than one-sixth of the CPU time and less than one-third of the memory. All the pictures that show the flow field around the cylinder display the part of the domain enclosed by the rectangular region with the lower left and upper right corners located at (13, 10) and (43, 22) respectively. Some of the data from these computations were used to produce a set of video animations[23] to have a better understanding of these unsteady flows involving oscillating cylinders.

4.1.1. Forced horizontal oscillations of a cylinder at Reynolds number 100. It is well known that at Reynolds number 100 flow past a fixed cylinder leads to the classical unsymmetrical vortex shedding. In such a case the lift and torque coefficients oscillate with a frequency corresponding to the related Strouhal number, while the drag oscillates with twice that frequency. The case in which the cylinder is subjected to forced horizontal oscillations shows some interesting features. Depending on the amplitude and frequency (f_f) of the forced oscillations of the cylinder, two modes of vortex shedding are possible. This phenomenon, for vortex-induced oscillations, has been discussed in the review papers by Sarpkaya[10] and King.[11] Oscillations with a low reduced frequency ($F_f = 2f_f a/U_\infty$, where a is the radius of the cylinder and U_∞ is the freestream velocity) lead to unsymmetric modes of vortex shedding. For higher values of F_f, on the other hand, symmetric vortex shedding is observed. However, such a symmetric arrangement of the vortices is unstable and consequently the vortices coalesce and eventually become unsymmetrical downstream.

We simulate the flow with symmetrical shedding by forcing the cylinder to oscillate horizontally with the prescribed displacement (normalized by the cylinder radius)

$$X = 1 - \cos(\omega_f t), \tag{20}$$

where $\omega_f = 2\pi f_f$. For this case the value of f_f corresponds to a reduced frequency of 0·35. The initial condition for this simulation is prescribed as the temporally periodic solution for flow past a fixed cylinder at $Re = 100$. Figure 1 shows the time histories of the drag, lift and torque coefficients and the normalized horizontal displacement and velocity (normalized by the freestream velocity) of the cylinder. We observe that the drag coefficient for the horizontally oscillating cylinder is significantly larger than that for a fixed cylinder. Furthermore, the drag coefficient oscillates with a reduced frequency of 0·35 whereas the lift and torque coefficients approach zero. The fact that we start from an unsymmetric solution and still obtain a symmetric mode of shedding demonstrates that this mode is stable one. Figure 2 shows a sequence of frames for the vorticity field during one period of the cylinder motion. The first, third and last frames correspond to the mean cylinder location, while the second and fourth frames correspond to the left and right extreme positions of the cylinder respectively. It can be observed that during each period of cylinder motion two symmetrical pairs of vortices are shed from the cylinder's lower and upper surfaces. One of these pairs is shed while the cylinder moves in the direction of the flow (i.e. while the relative Reynolds number for the cylinder is < 100) whereas the other one is shed while the cylinder motion opposes the freestream flow (i.e. while the relative Reynolds number for the cylinder is > 100). The former pair is much weaker than the latter and diffuses very quickly.

4.1.2. Vortex-induced vertical oscillations of a cylinder. Unsymmetrical vortex shedding causes a fixed cylinder to experience an alternating lift force at a frequency corresponding to the Strouhal number for that Reynolds number. If the cylinder is mounted on a flexible support, then under certain conditions it can undergo sustained oscillations with a frequency close to or coincident with its natural frequency. These oscillations can alter the vortex-shedding mechanism, which in turn can change the cylinder response, and so on. This leads to a complex non-linear fluid–structure interaction phenomenon and has been the subject of several investigations.[9–18]

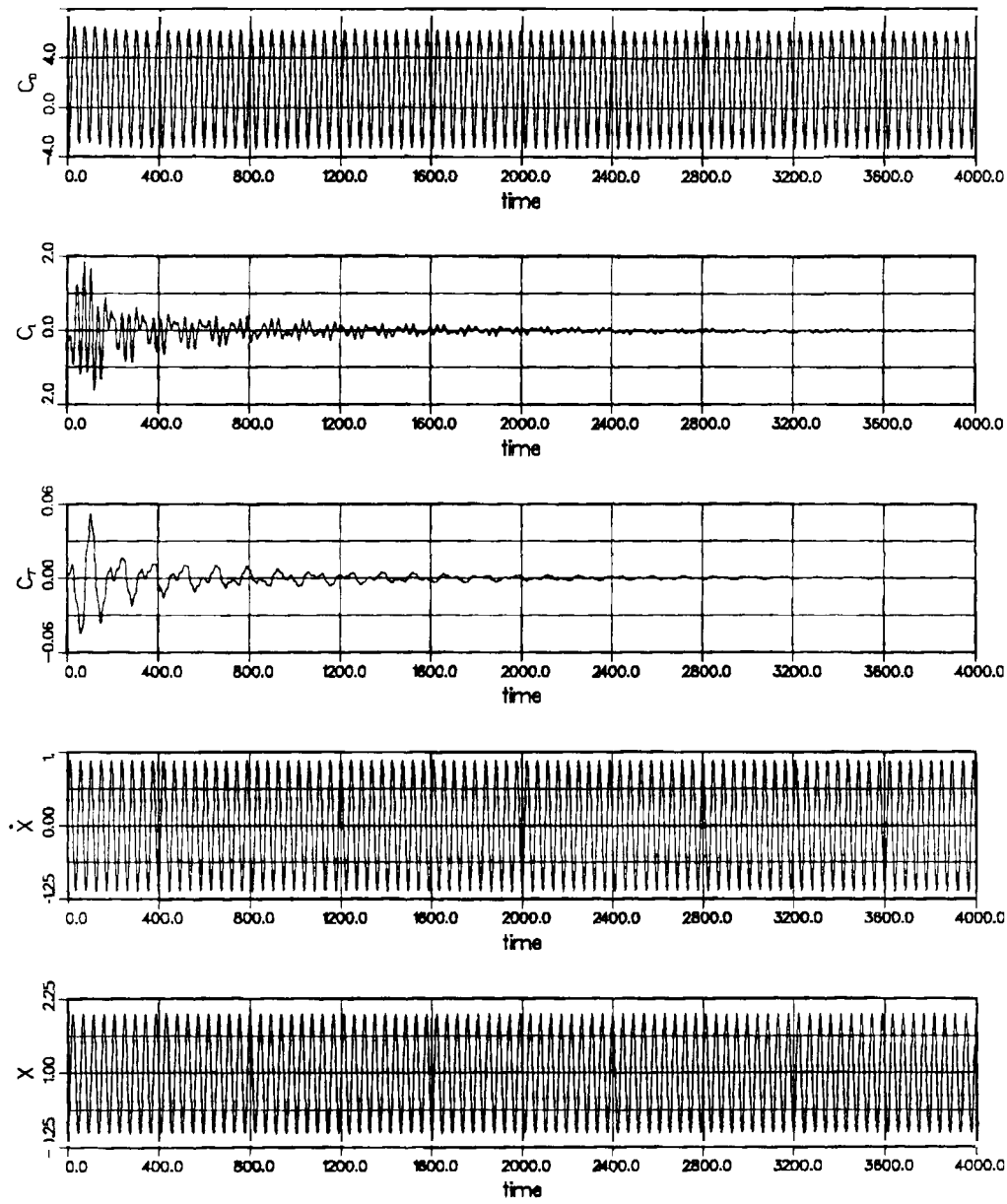

Figure 1. Flow past a horizontally oscillating cylinder at $Re = 100$: time histories of the drag, lift and torque coefficients and the normalized velocity and displacement of the cylinder

We simulate this phenomenon for a cylinder which is allowed to move only in the vertical direction. The motion of the cylinder is governed by

$$\ddot{Y} + 2\pi F_n \zeta \dot{Y} + (\pi F_n)^2 Y = \frac{C_L}{M}. \tag{21}$$

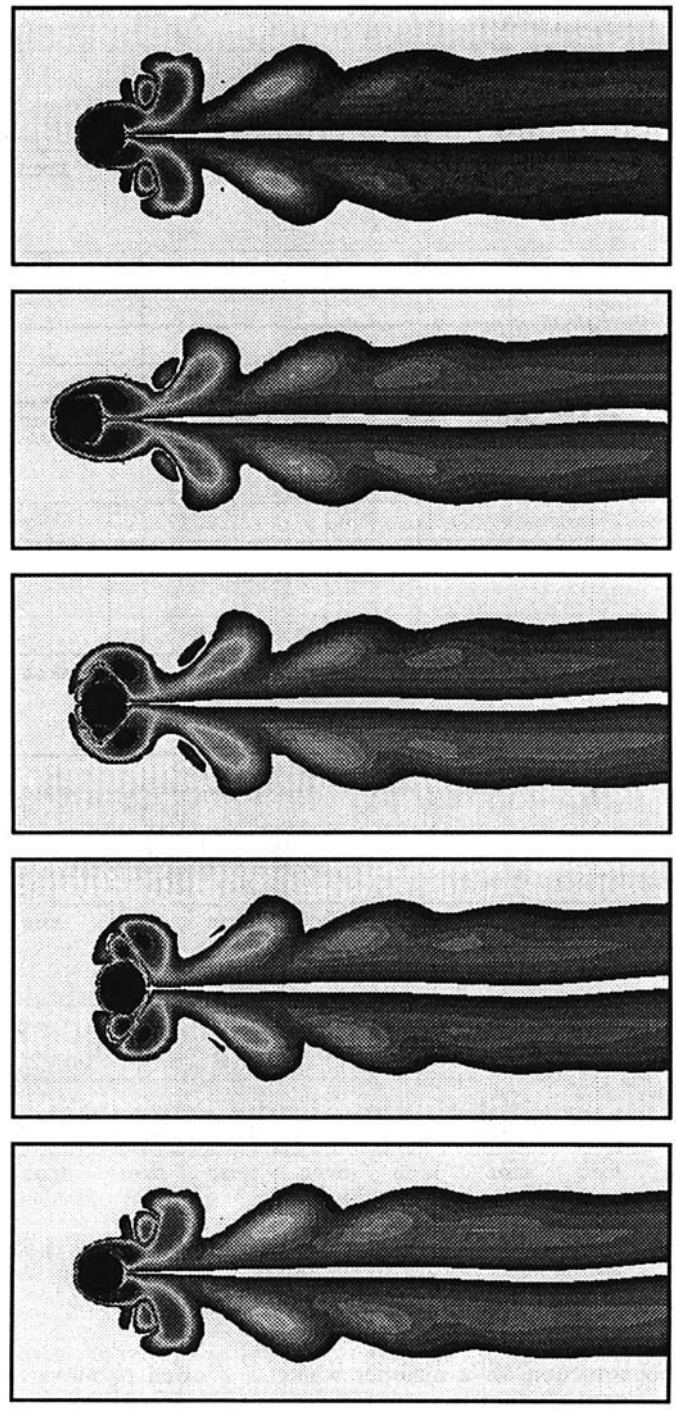

Figure 2. Flow past a horizontally oscillating cylinder at $Re = 100$: vorticity at various instants during one period of the cylinder motion

Here $\ddot{Y}$, $\dot{Y}$ and Y are the normalized vertical acceleration, velocity and displacement of the cylinder respectively. The displacement and velocity of the cylinder are normalized by its radius and the freestream velocity respectively. M is the non-dimensional mass/unit length of the cylinder, ζ is the structural damping coefficient associated with the system and C_L denotes the lift coefficient for the cylinder. F_n, the reduced natural frequency of the spring–mass system, is defined as

$$F_n = \frac{2f_n a}{U_\infty}, \tag{22}$$

where f_n is the actual natural frequency of the system. Equation (22) can be rewritten as

$$F_n = \frac{4f_n a^2 \rho}{\mu} \frac{1}{Re}. \tag{23}$$

For our problem, $F_n = 66/Re$, $M = 472{\cdot}74$ and $\zeta = 3{\cdot}3 \times 10^{-4}$.

Reynolds number = 324. At Reynolds number 324 the reduced natural frequency of the spring–mass system and the Strouhal number for flow past a fixed cylinder have very close values. Therefore we decided to first carry out this simulation for Reynolds number 324. The temporally periodic solution for flow past a fixed cylinder at the same Reynolds number is used as the initial condition. Time histories of the drag, lift and torque coefficients for the fixed cylinder at $Re = 324$ are shown in Figure 3. Figure 4 shows a sequence of frames for the vorticity during one period of the lift coefficient for the fixed cylinder. Figure 5 shows, for the initial and later stages of the

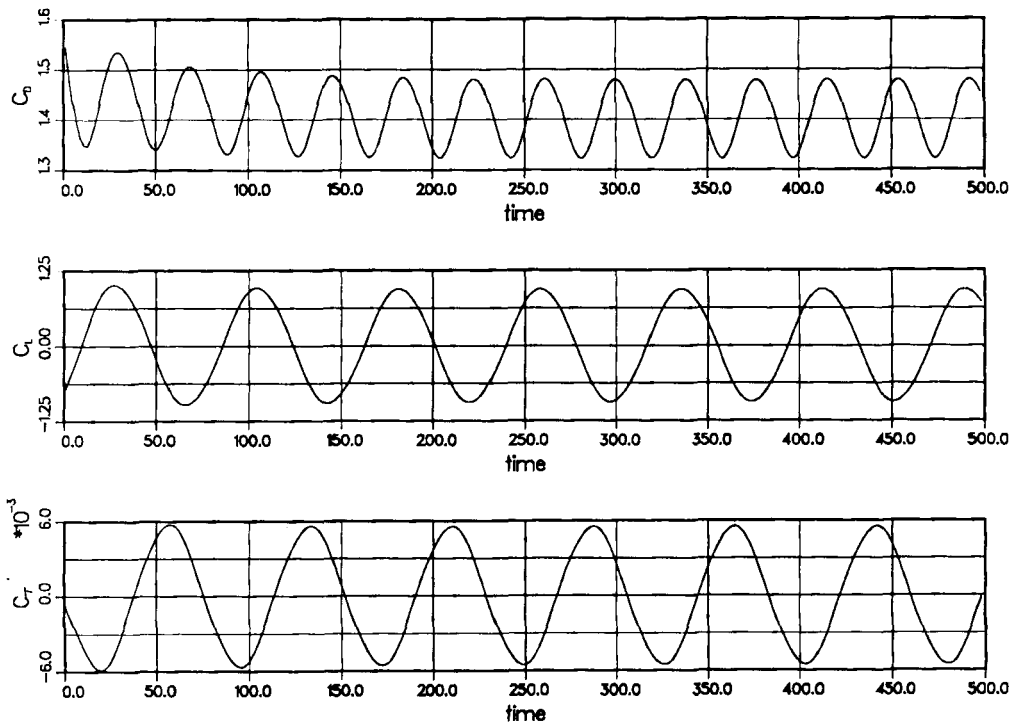

Figure 3. Flow past a fixed cylinder at $Re = 324$: time histories of the drag, lift and torque coefficients

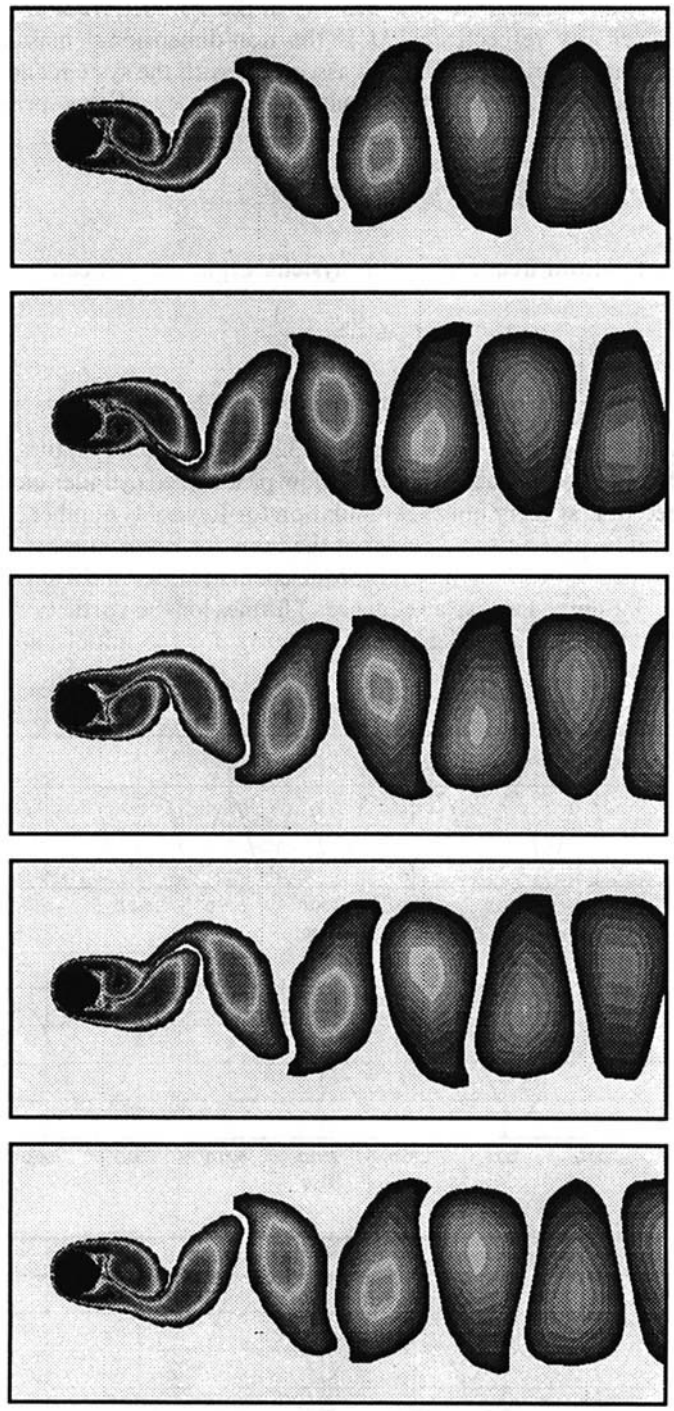

Figure 4. Flow past a fixed cylinder at $Re = 324$: vorticity at various instants during one period of the lift coefficient

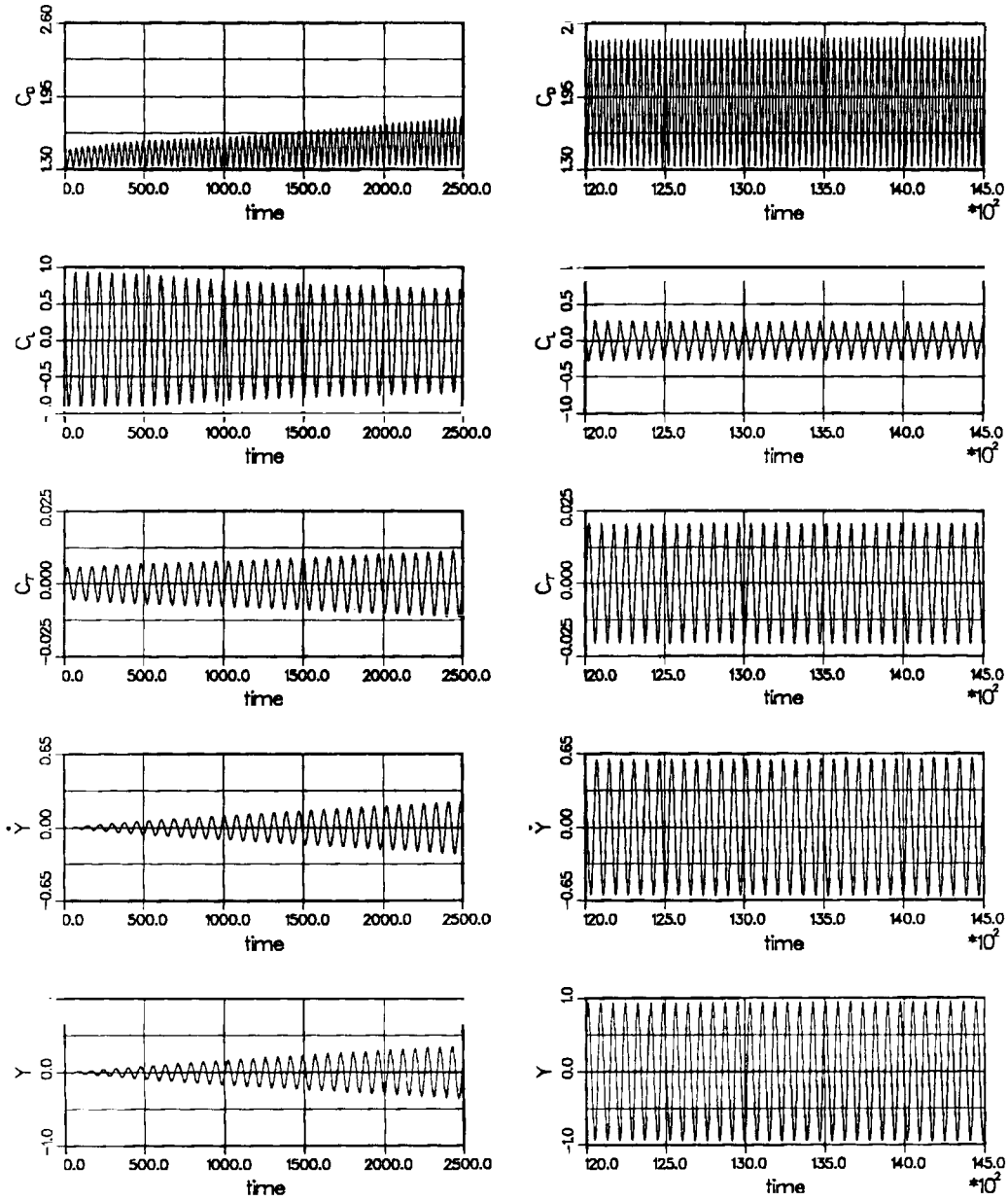

Figure 5. Flow past a vertically oscillating cylinder at $Re = 324$: initial and later time histories of the drag, lift and torque coefficients and the normalized velocity and displacement of the cylinder

simulation, time histories of the drag, lift and torque coefficients and the normalized vertical displacement and velocity of the cylinder. We observe that initially the cylinder oscillates with an increasing amplitude. The drag and torque coefficients for the cylinder also increase, while the lift coefficient has a decreasing amplitude. It is interesting to note that both the mean and peak values of the drag coefficient increase with time but the trough value remains almost constant. Later, the

cylinder reaches a temporally periodic oscillation amplitude of approximately one radius. It oscillates with its natural frequency and so does the torque coefficient; the drag coefficient oscillates with twice the natural frequency of the cylinder. The dominant frequency for the lift coefficient corresponds to the natural frequency of the cylinder. In addition, there is a very small component of the lift coefficient with thrice the frequency of the dominant one (see the power spectra in Figure 6). Figure 7 shows a sequence of frames for the vorticity field during one period of the cylinder motion. The first, third and last frames correspond to the mean cylinder location, while the second and fourth frames correspond to the lower and upper extreme positions of the cylinder respectively. The finite element meshes corresponding to the lower extreme, mean and upper extreme positions of the cylinder are shown in Figure 8.

Variation of cylinder response with Reynolds number. We also investigated the behaviour of this non-linear oscillator at Reynolds numbers for which the Strouhal number for the flow past a fixed cylinder (F_{s0}) is different from the reduced natural frequency of the spring–mass system (F_n). For later reference we define F_s to be the Strouhal number for the flow past an oscillating cylinder. Figure 9 shows the response of the cylinder at various Reynolds numbers. We observe that for certain ranges of the Reynolds number the temporally periodic oscillation amplitude of the cylinder reaches two different values depending on the initial condition. For those Reynolds numbers an initial condition corresponding to a low oscillation amplitude of the cylinder leads to a temporally periodic solution with a low amplitude of vibration. On the other hand, if the initial condition corresponds to an oscillation amplitude that is higher than a certain threshold value, which we will discuss later, a temporally periodic solution with a high amplitude of cylinder vibration is reached. We will refer to these two different types of solutions as the low- and high-amplitude solutions. These double-amplitude solutions of the oscillator can also be interpreted as a 'hysteresis'-type behaviour; the oscillator reaches different vibration amplitudes depending on whether one approaches the Reynolds number of interest from a lower or a higher side. The cause of this behaviour will be discussed later in the paper. For the set of Reynolds number studied, there is also a range for which only one level of oscillation amplitude is obtained regardless of the initial condition. We will refer to these solutions too as the high-amplitude solutions. Figure 10 shows the variation with Reynolds number of the different non-dimensional frequencies associated with the system. Also plotted in the same figure are the experimental values of the Strouhal number, obtained by Roshko (extracted from Reference 13), for flow past a fixed cylinder at different Reynolds numbers. This relation is given as

$$F_{s0} = 0{\cdot}212\left(1 - \frac{12{\cdot}7}{Re}\right). \tag{24}$$

It can be seen that for flow past a fixed cylinder the difference between the Strouhal number from our computations and the one given by equation (24) is less than 3%. We also observe from our computations that for all the Reynolds numbers we studied, for high-amplitude solutions the vortex-shedding frequency of the oscillating cylinder becomes equal to the natural frequency of the system (i.e. $F_s = F_n$). This phenomenon has been observed by several other researchers in the past and is known as 'lock-in'.[9–16] For the range of Reynolds numbers for which we observe multiple solutions, the low-amplitude solution results in a Strouhal number very close to the one for a fixed cylinder. We will first describe the cases for which $F_n < F_{s0}$ (i.e. $Re > 324$).

Reynolds number >324. Figure 11 shows for Reynolds number 330 the initial and later time histories of the drag, lift and torque coefficients and the normalized vertical displacement and velocity of the cylinder. We observe that the response of the cylinder is very similar to the one for Reynolds number 324.

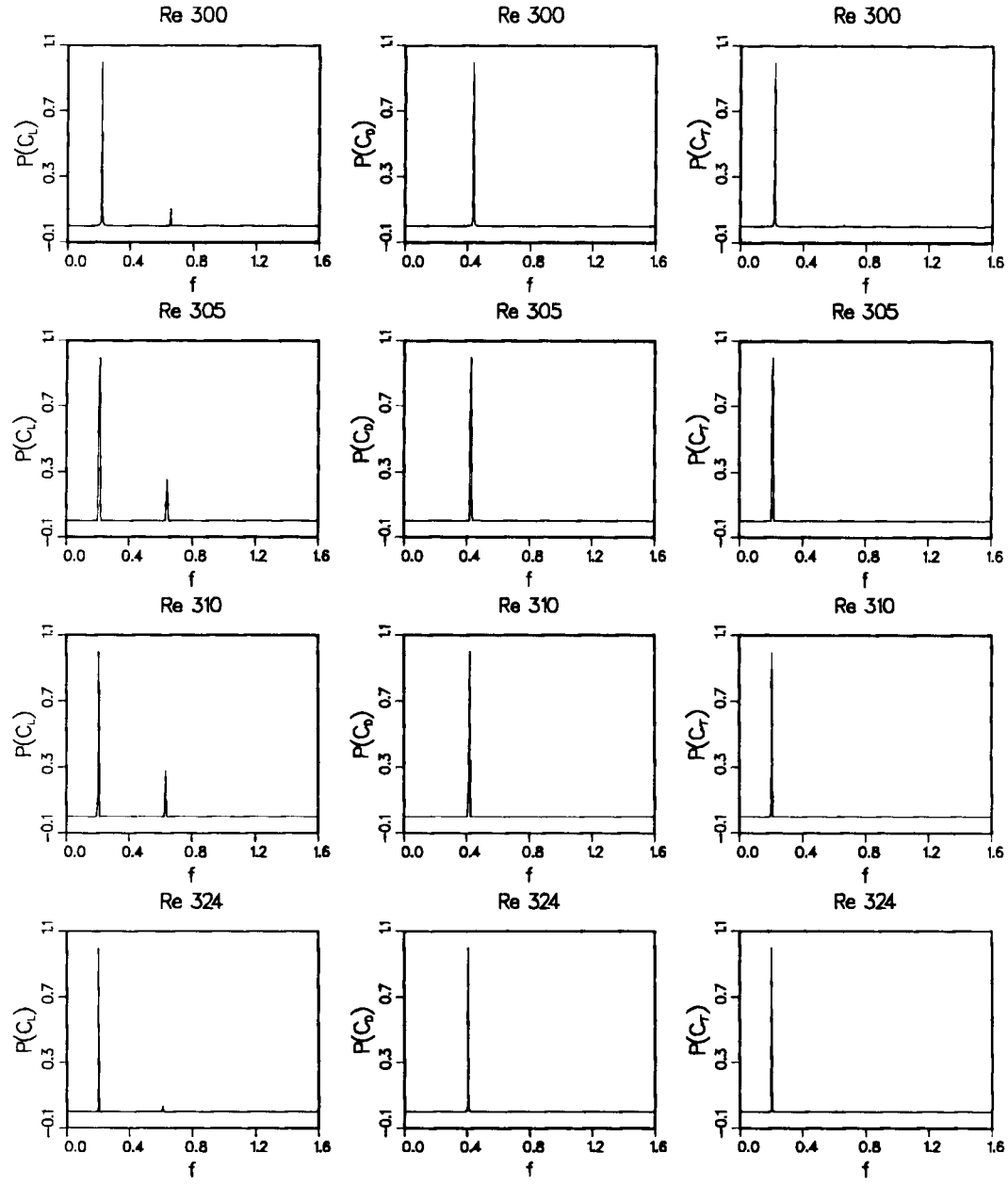

Figure 6. Flow past a vertically oscillating cylinder: power spectra of the lift, drag and torque coefficients at different Reynolds numbers

For Reynolds number 340 we obtain two solutions depending on the initial oscillation amplitude of the cylinder. The initial and later time histories of the drag, lift and torque coefficients and the normalized vertical displacement and velocity of the cylinder for the low-amplitude solution are shown in Figure 12. We observe 'beats' in the response of the cylinder during the initial stages of the simulation. Finally, the cylinder reaches a temporally periodic

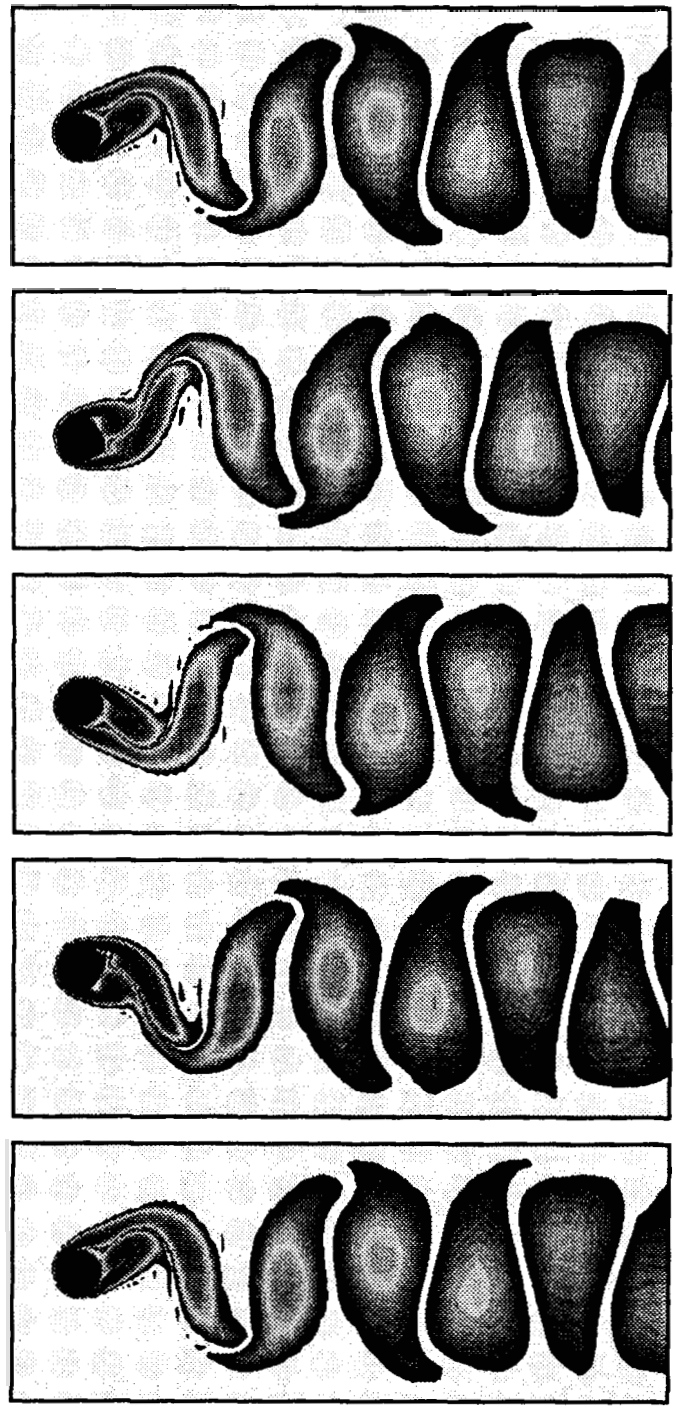

Figure 7. Flow past a vertically oscillating cylinder at $Re = 324$: vorticity at various instants during one period of the cylinder motion

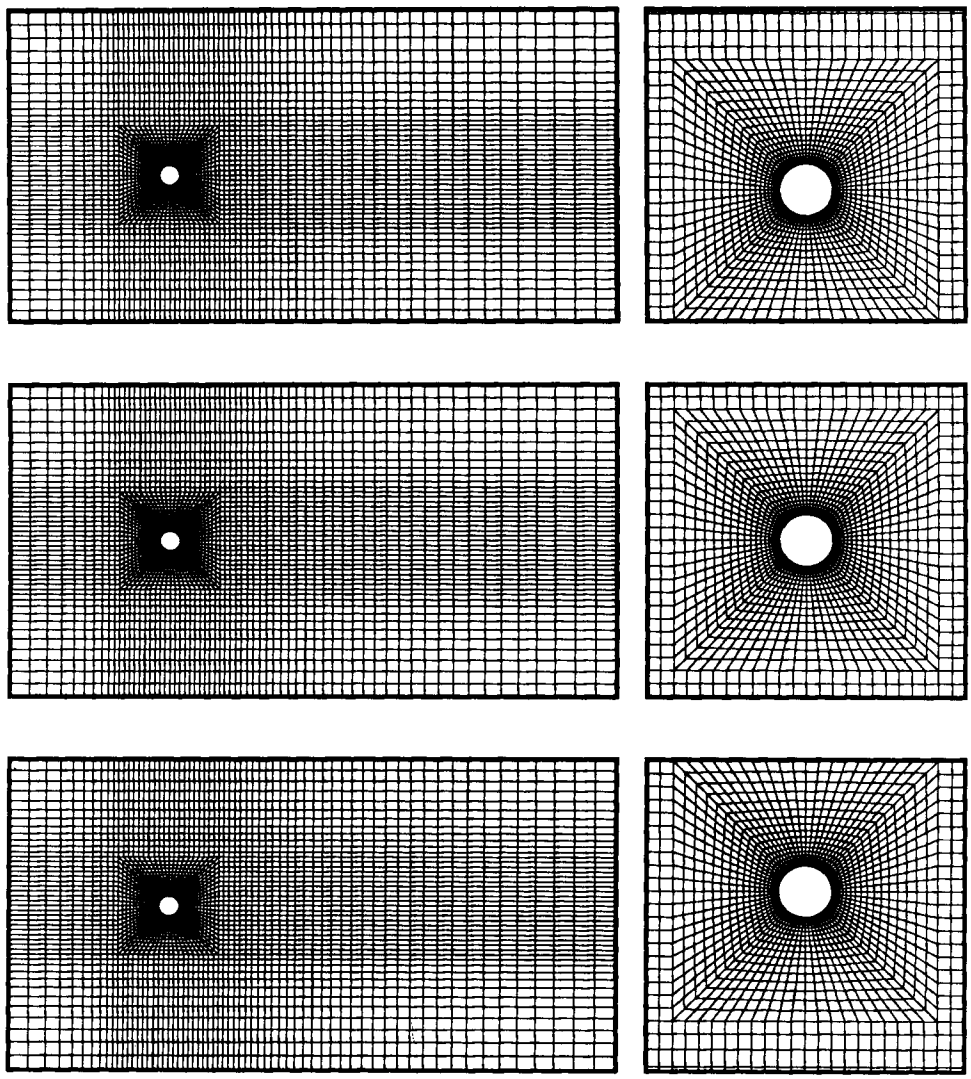

Figure 8. Flow past a vertically oscillating cylinder at $Re = 324$: finite element meshes corresponding to the lowest, mean and highest positions of the cylinder

vibration amplitude of approximately 0·03 radii. Corresponding to this low-amplitude solution, Figure 13 shows a sequence of frames for the vorticity during one period of the cylinder motion. These flow patterns look very similar to those in Figure 4 for a fixed cylinder at Reynolds number 324. Figure 14 shows for the high-amplitude solution the time histories of the drag, lift and torque coefficients and the normalized vertical displacement and velocity of the cylinder. The corresponding flow fields during one period of the cylinder motion are shown in Figure 15. When we compare Figures 13 and 15, we notice that the longitudinal spacing between the vortices for the high-amplitude solution is larger than that for the low-amplitude solution. The wake behaves this way because for the high-amplitude solution the shedding frequency gets locked in to the natural

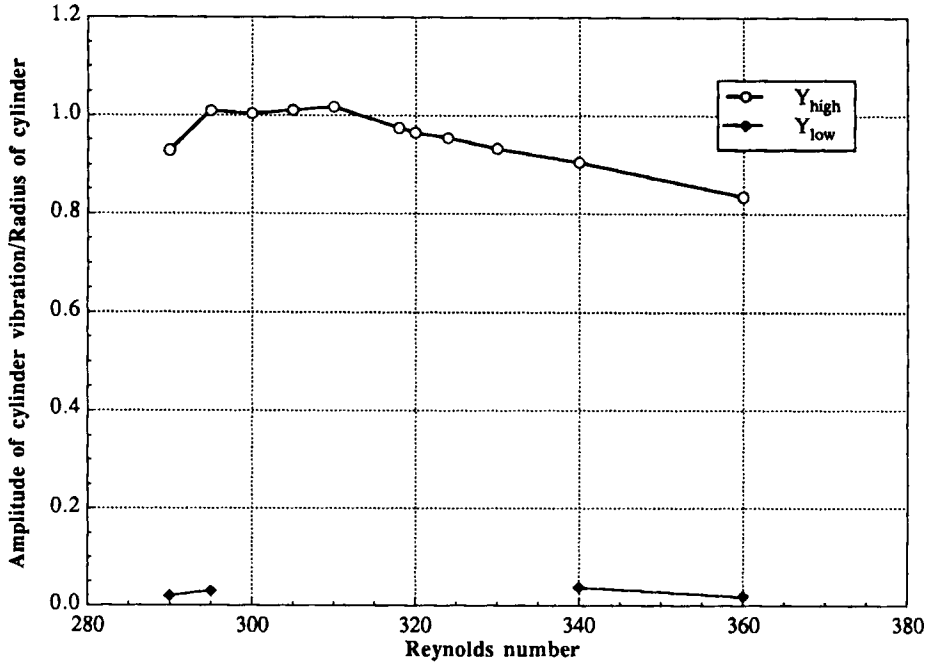

Figure 9. Flow past a vertically oscillating cylinder: non-dimensional oscillation amplitude versus Reynolds number

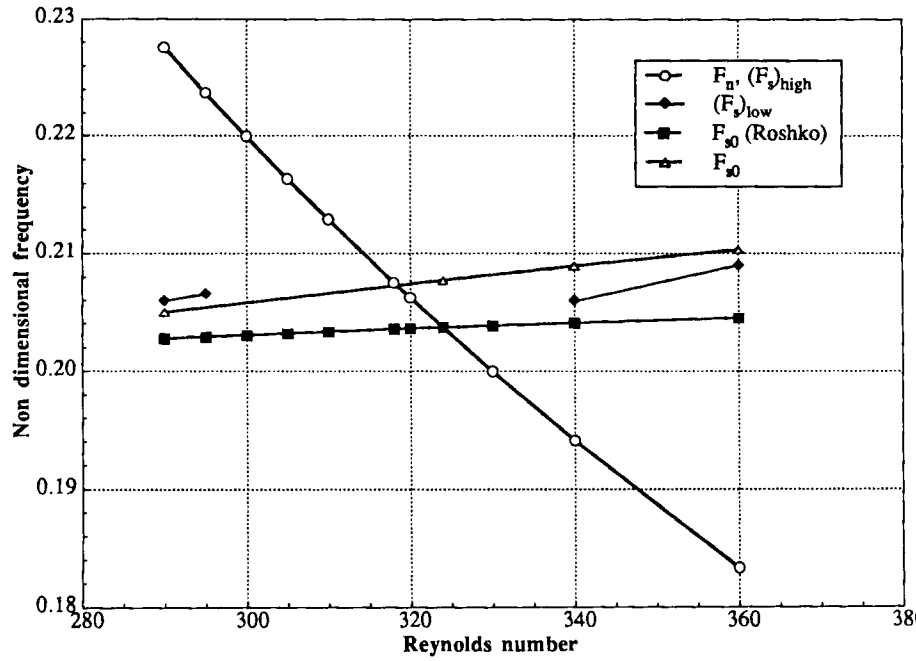

Figure 10. Flow past a vertically oscillating cylinder: non-dimensional frequency versus Reynolds number

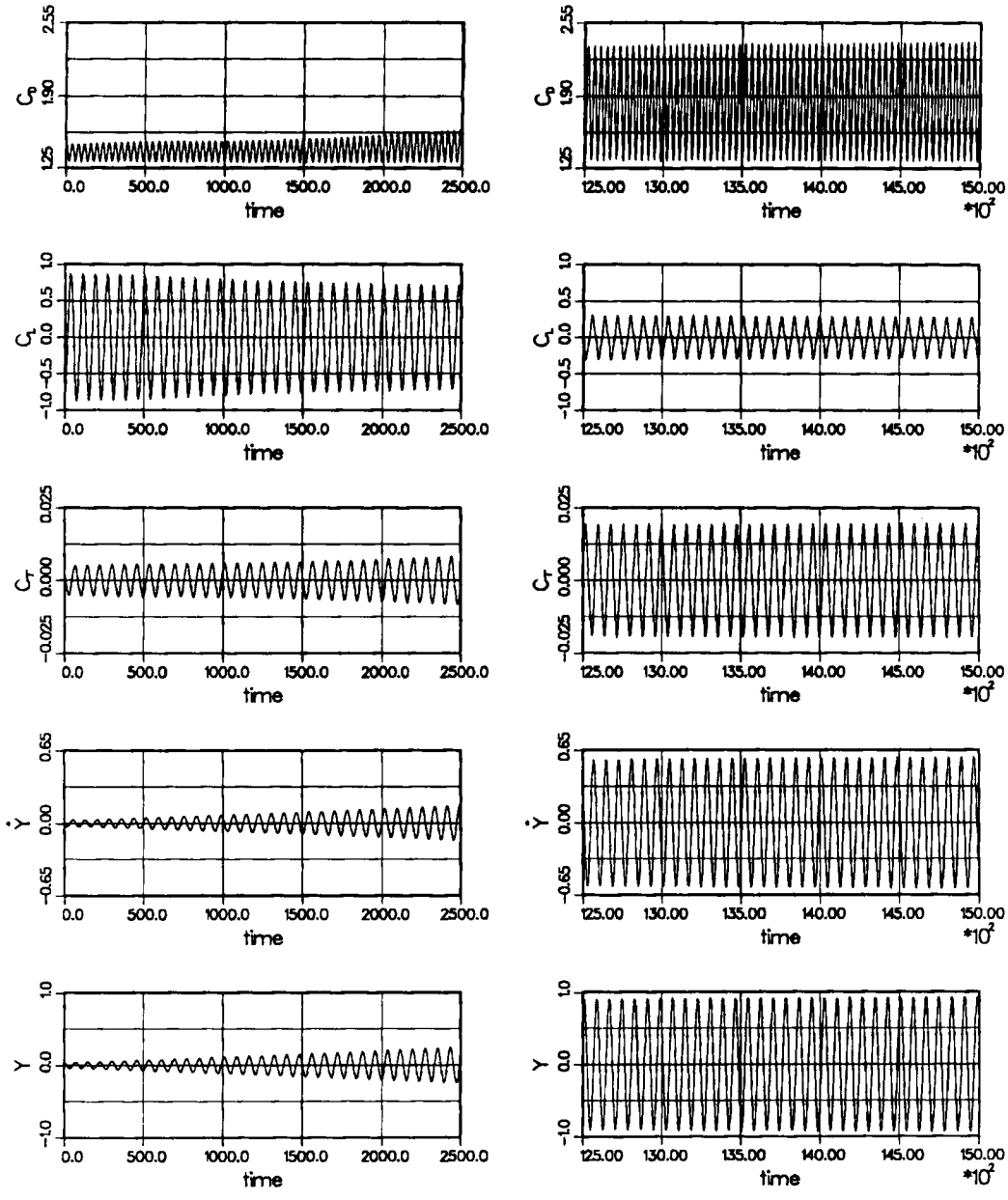

Figure 11. Flow past a vertically oscillating cylinder at $Re = 330$: initial and later time histories of the drag, lift and torque coefficients and the normalized velocity and displacement of the cylinder

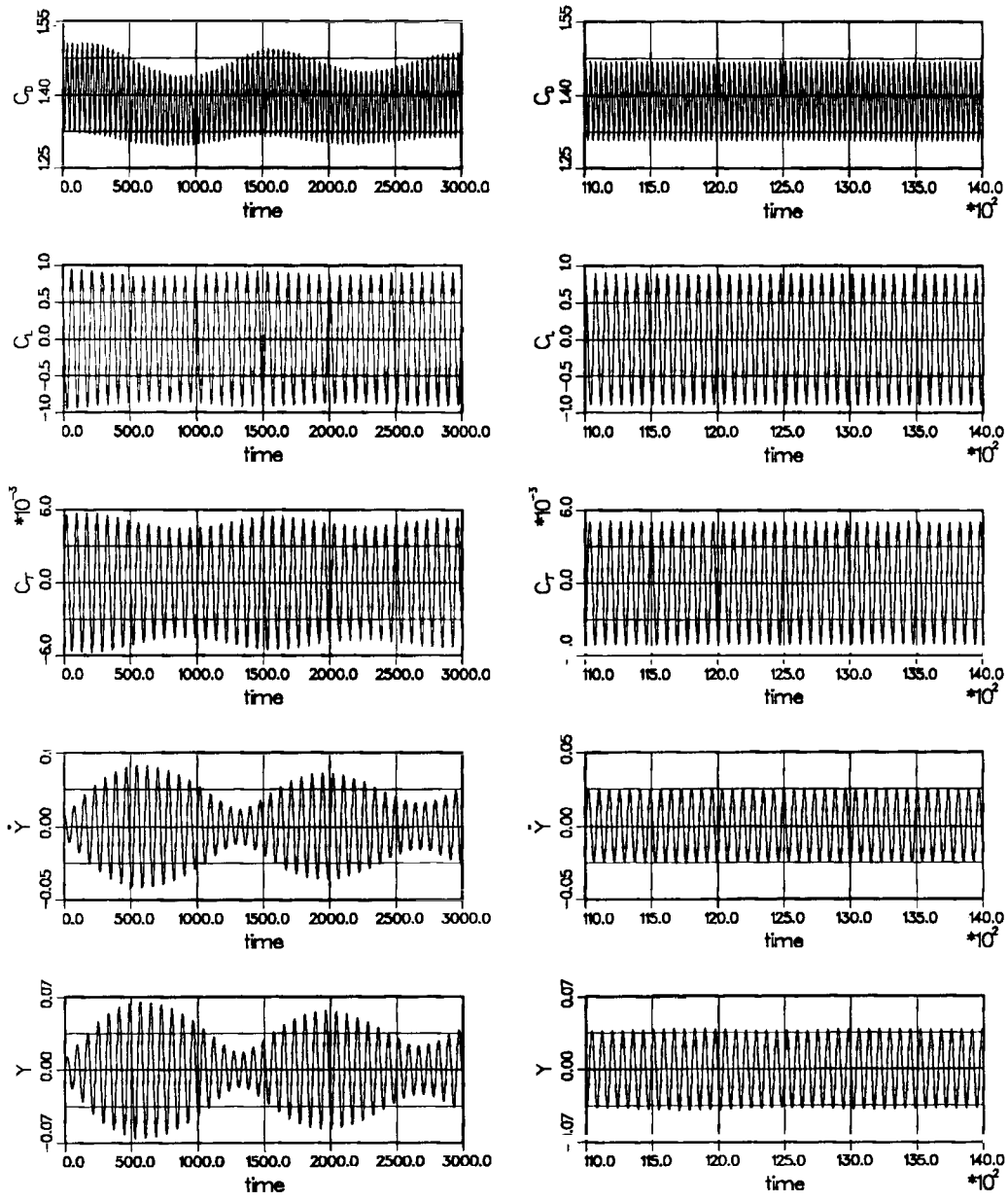

Figure 12. Flow past a vertically oscillating cylinder at $Re = 340$ (low-amplitude solution): initial and later time histories of the drag, lift and torque coefficients and the normalized velocity and displacement of the cylinder

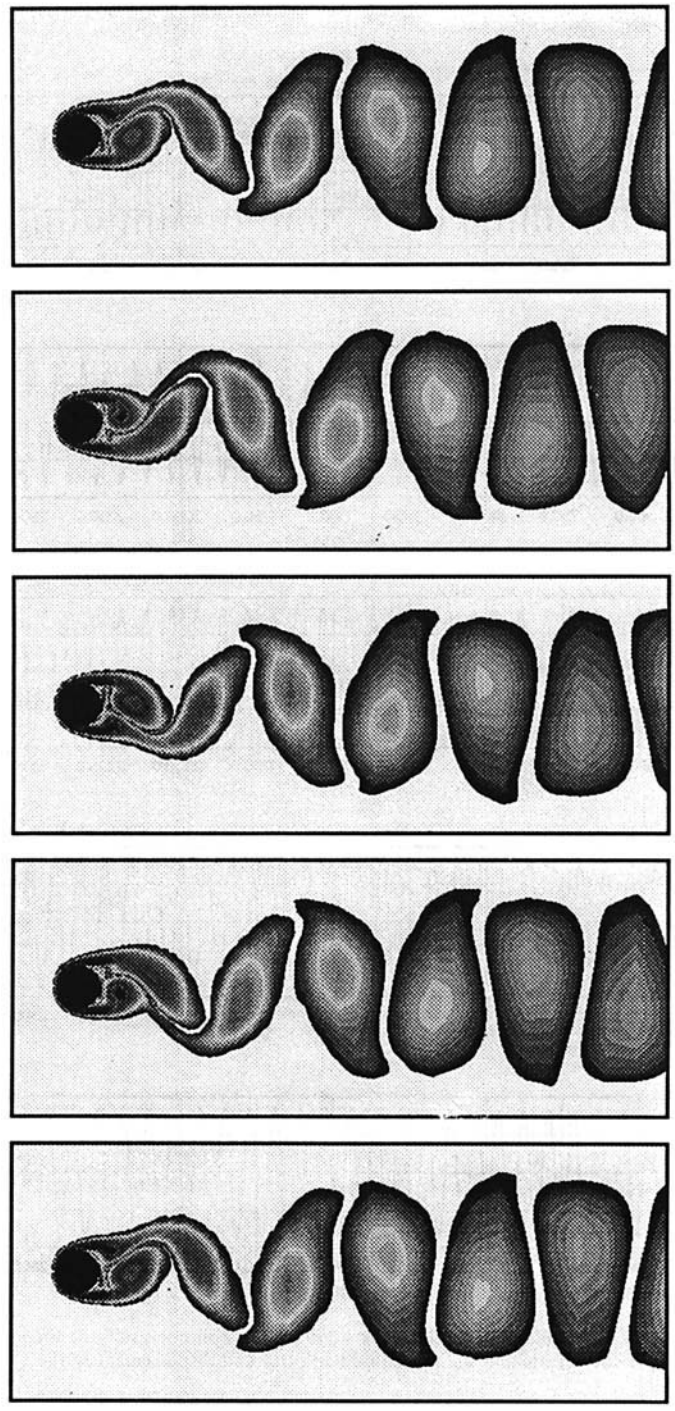

Figure 13. Flow past a vertically oscillating cylinder at $Re = 340$ (low-amplitude solution): vorticity at various instants during one period of the cylinder motion

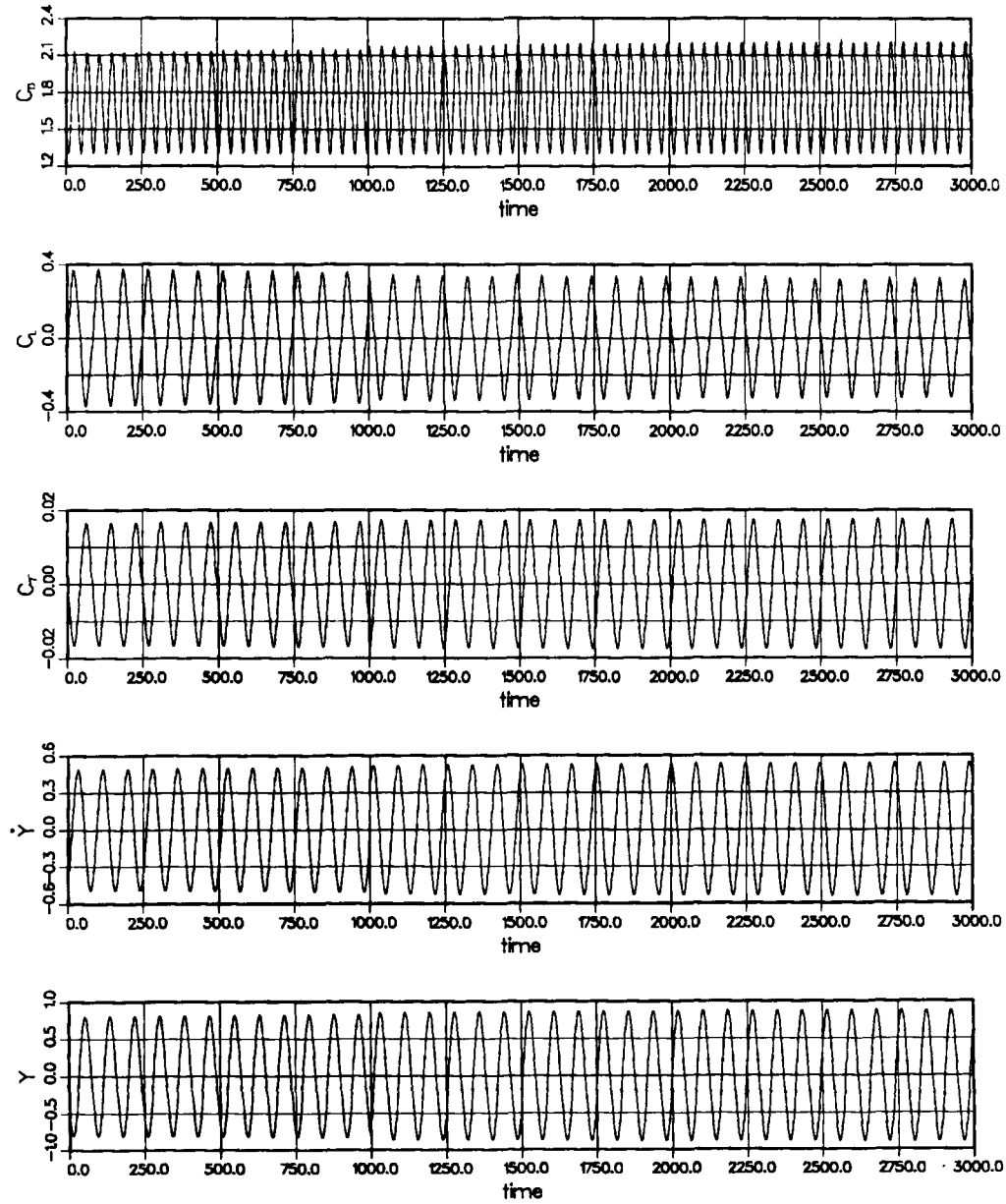

Figure 14. Flow past a vertically oscillating cylinder at $Re = 340$ (high-amplitude solution): time histories of the drag, lift and torque coefficients and the normalized velocity and displacement of the cylinder

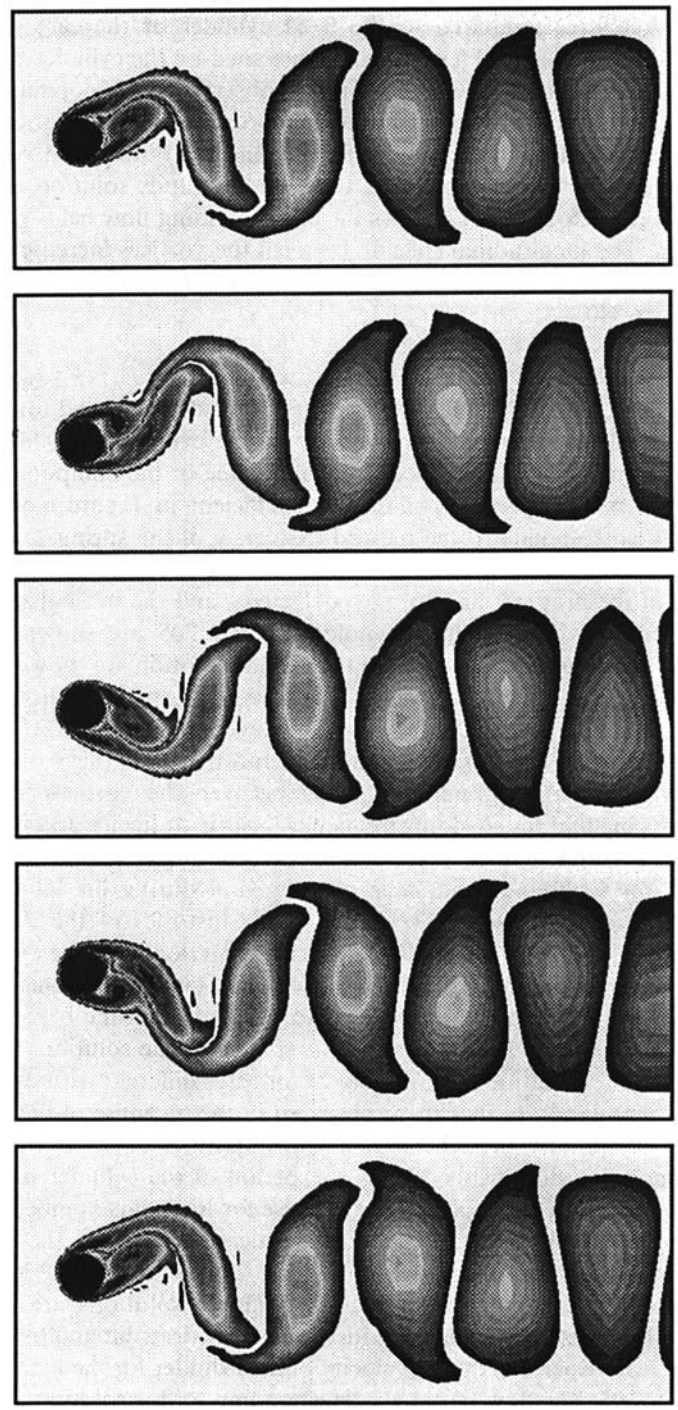

Figure 15. Flow past a vertically oscillating cylinder at $Re = 340$ (high-amplitude solution): vorticity at various instants during one period of the cylinder motion

frequency, whereas the shedding frequency for the low-amplitude solution is very close to that for a fixed cylinder. Therefore, compared to the fixed cylinder or the case with low-amplitude oscillations, in a given time interval fewer vortices are shed by the cylinder with high-amplitude oscillations ($F_n < F_{s0}$). The same phenomenon was observed by Koopmann[12] as a result of conducting a set of laboratory experiments involving forced vertical oscillations of cylinders. The time histories of the drag, lift and torque coefficients and the normalized vertical displacement and velocity of the cylinder corresponding to the high-amplitude solution at Reynolds number 360 are shown in Figure 16. Figure 17 shows the corresponding flow fields during one period of the cylinder motion. The longitudinal spacing between the vortices increases even more for this case. This is expected because the difference between F_{s0} and F_n is higher for this case than it was for Reynolds number 340.

Reynolds number < 324. Now we describe the cases for which $F_n > F_{s0}$ (i.e. $Re < 324$). Figure 18 shows for Reynolds number 310 the time histories of the drag, lift and torque coefficients and the normalized vertical displacement and velocity of the cylinder. The lift coefficient has an additional temporal frequency that reduces the peak value of the component at the dominant frequency. From the power spectrum of the lift coefficient in Figure 6 we observe that the dominant frequency corresponds to the natural frequency of the spring–mass system and that there is an additional component at $3F_n$. Similar results are observed for Reynolds number 305. The time histories of the drag, lift and torque coefficients and the normalized vertical displacement and velocity of the cylinder for Reynolds number 305 are shown in Figure 19. The corresponding flow fields during one period of the cylinder motion are shown in Figure 20. It can be seen that the longitudinal spacing between the vortices in the wake of the cylinder for this case is smaller than that for a fixed cylinder (e.g. for Reynolds number 324 in Figure 4). This arrangement of the vortices appears to be unstable and therefore the vortices coalesce downstream. The decrease in the longitudinal spacing between the vortices for this case can be explained by recognizing that the shedding frequency locks in to the natural frequency. Therefore, compared to a fixed cylinder, in a given time interval a larger number of vortices are shed ($F_n > F_{s0}$). Koopmann[12] observed the same phenomenon during his laboratory experiments involving cylinders forced to oscillate vertically. Time histories of the drag, lift and torque coefficients and the normalized vertical displacement and velocity of the cylinder for Reynolds number 300 are shown in Figure 21. The response of the cylinder for this case is particularly interesting because this Reynolds number seems to be the borderline between those for which multiple solutions are seen and those for which there is only one solution. Figure 22 shows the detailed plots of the same quantities as in Figure 21 for three different periods of time. During the initial stages of the simulation beats can be observed in the response of the cylinder. Later, the cylinder reaches a temporally periodic oscillation amplitude of approximately one cylinder radius. The corresponding flow fields during one period of the cylinder motion are shown in Figure 23. When we compare these pictures with those for Reynolds number 305 (Figure 20), we observe that the longitudinal spacing between the vortices decreases as the Reynolds number is decreased. We also notice that the disturbance that causes the vortices to coalesce travels upstream as the Reynolds number is decreased. Multiple solutions are observed for lower Reynolds numbers. Figure 24 shows the time histories of the drag, lift and torque coefficients and the normalized vertical displacement and velocity of the cylinder for the high-amplitude solution at Reynolds number 295. The flow patterns corresponding to this solution during one period of the cylinder motion are shown in Figure 25. The flow fields corresponding to the low-amplitude solution (not shown here) look very similar to those for flow past a fixed cylinder. For Reynolds number 290 the time histories of the drag, lift and torque coefficients and the normalized vertical

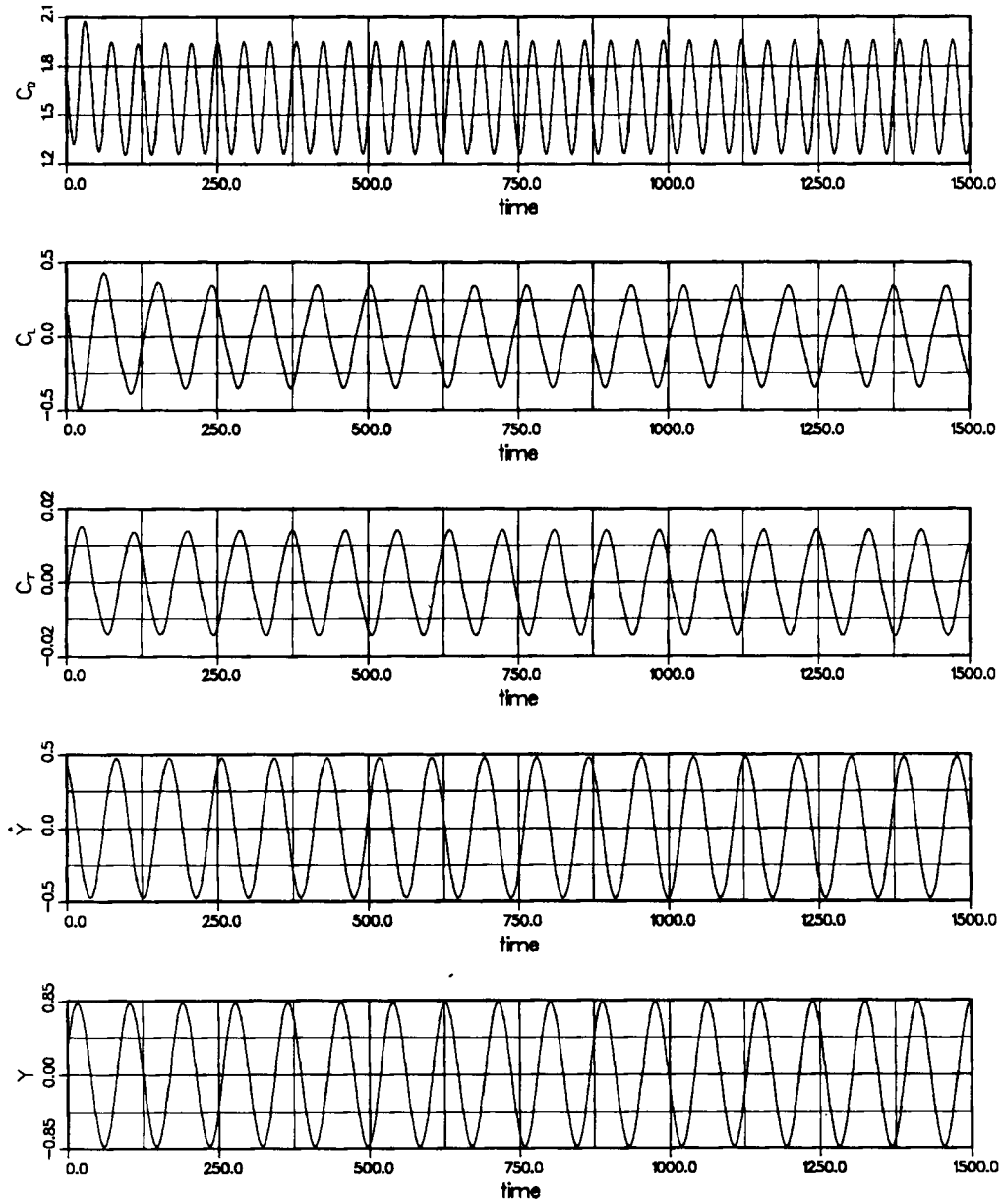

Figure 16. Flow past a vertically oscillating cylinder at $Re = 360$ (high-amplitude solution): time histories of the drag, lift and torque coefficients and the normalized velocity and displacement of the cylinder

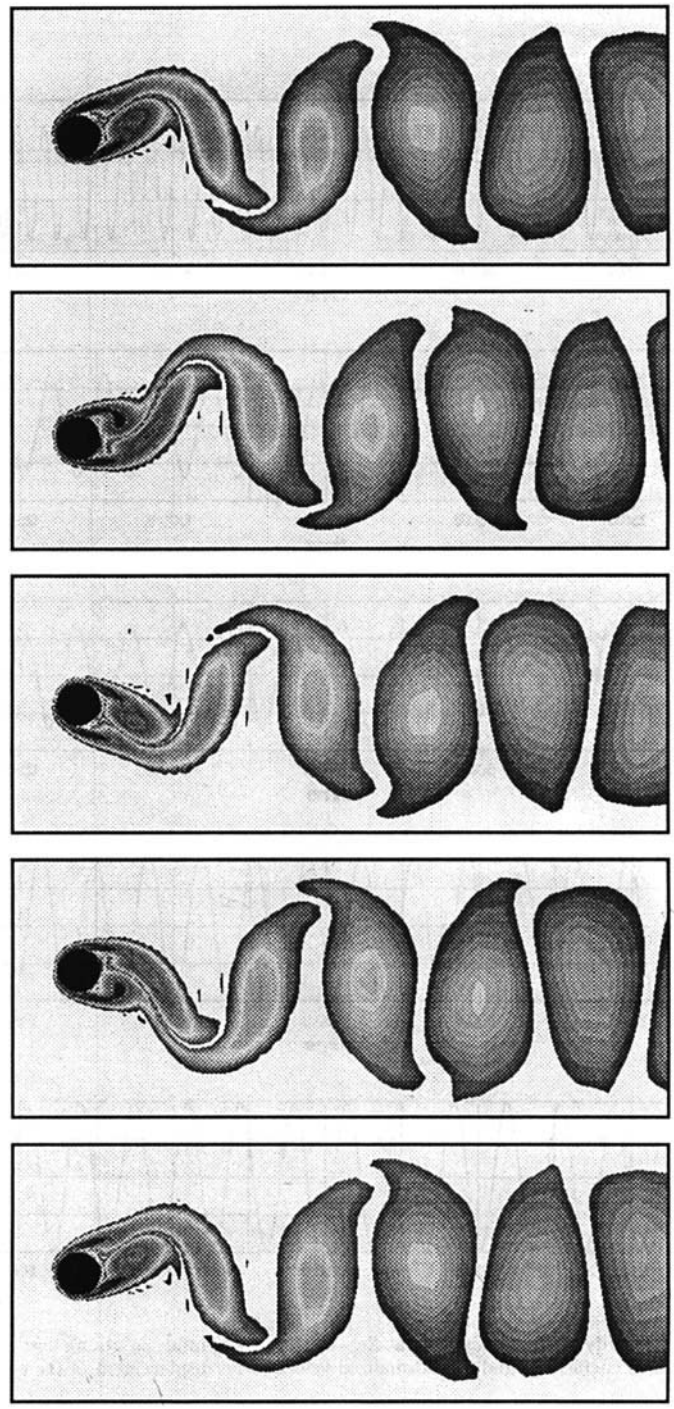

Figure 17. Flow past a vertically oscillating cylinder at $Re = 360$ (high-amplitude solution): vorticity at various instants during one period of the cylinder motion

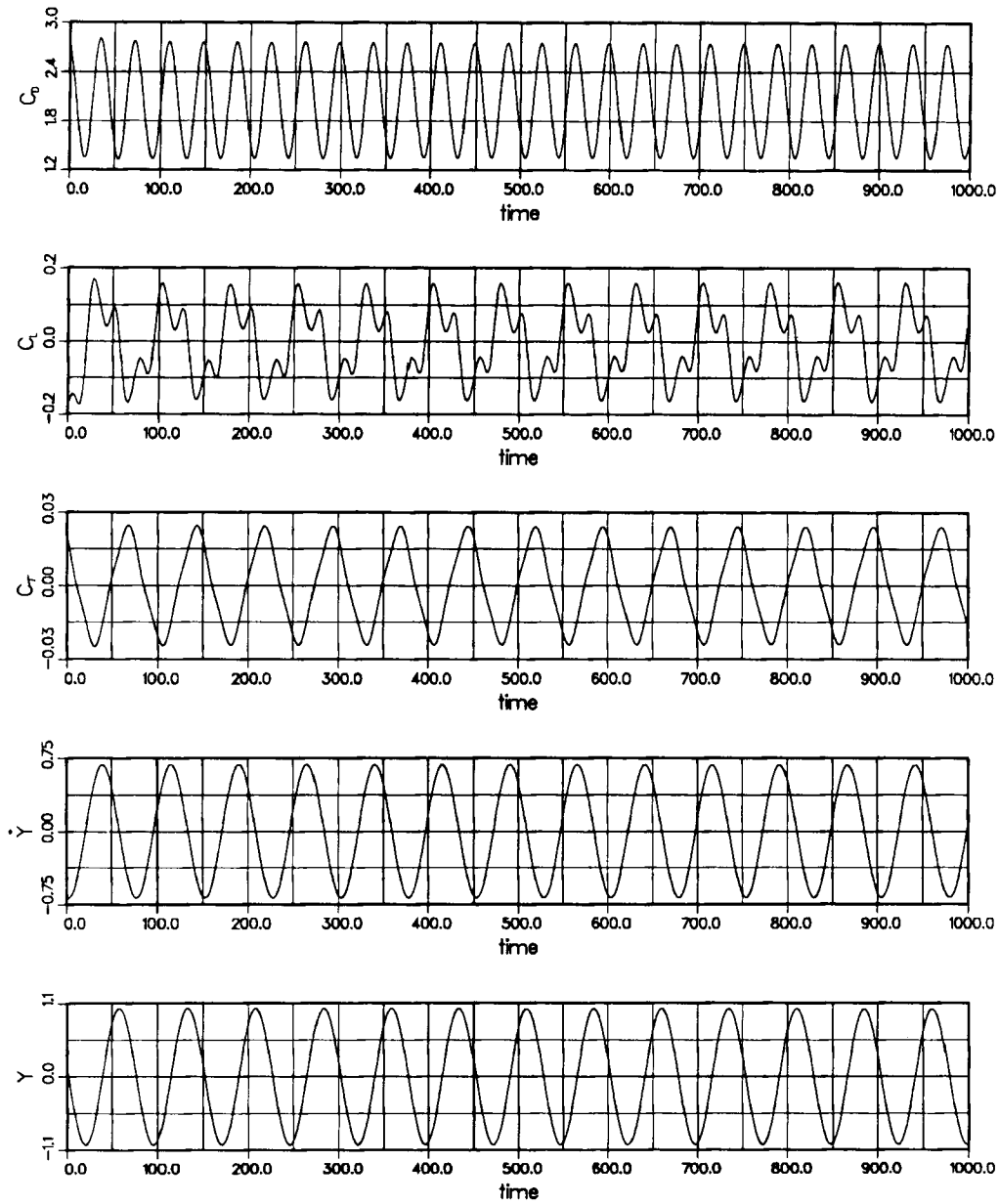

Figure 18. Flow past a vertically oscillating cylinder at $Re = 310$: time histories of the drag, lift and torque coefficients and the normalized velocity and displacement of the cylinder

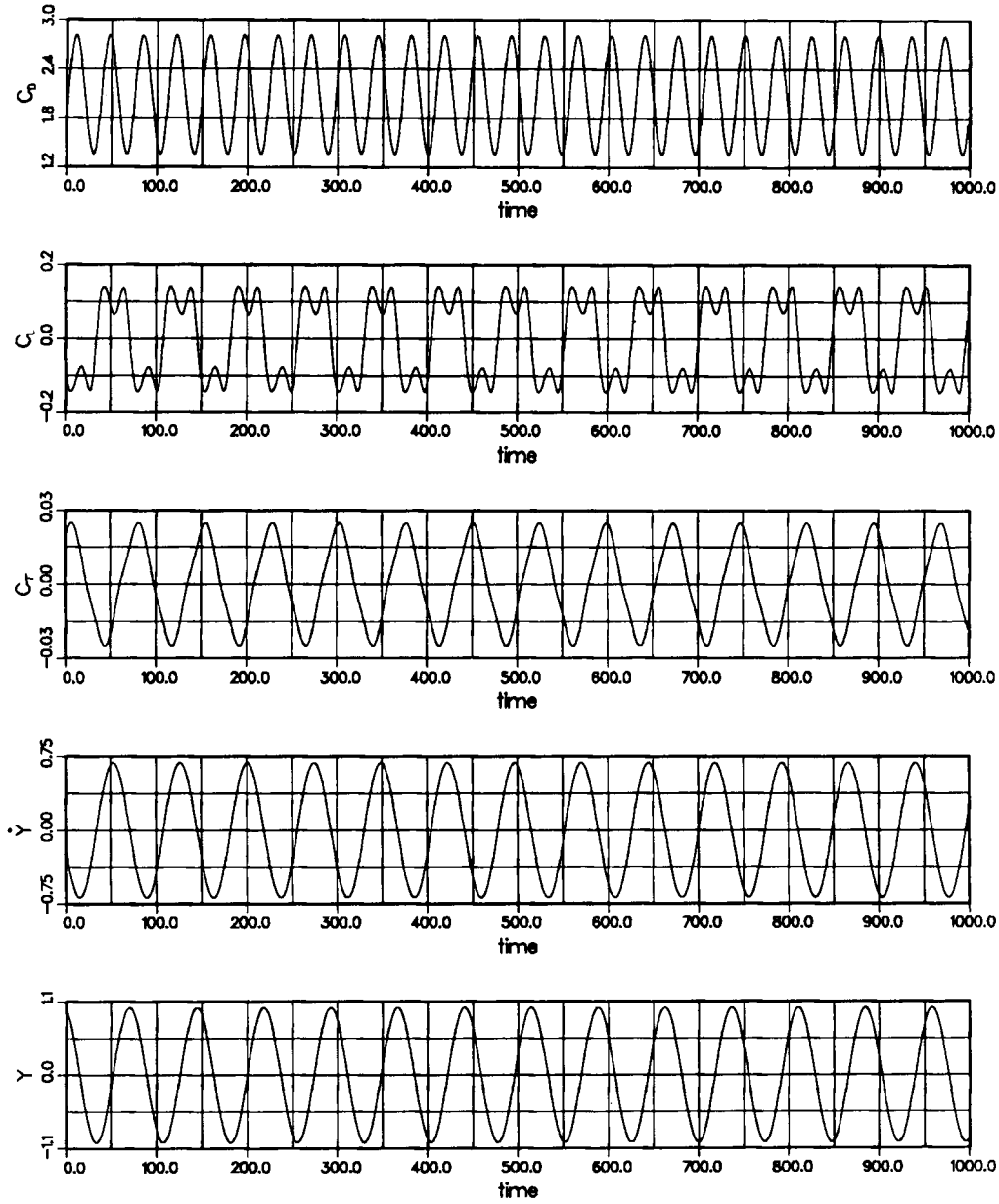

Figure 19. Flow past a vertically oscillating cylinder at $Re = 305$: time histories of the drag, lift and torque coefficients and the normalized velocity and displacement of the cylinder

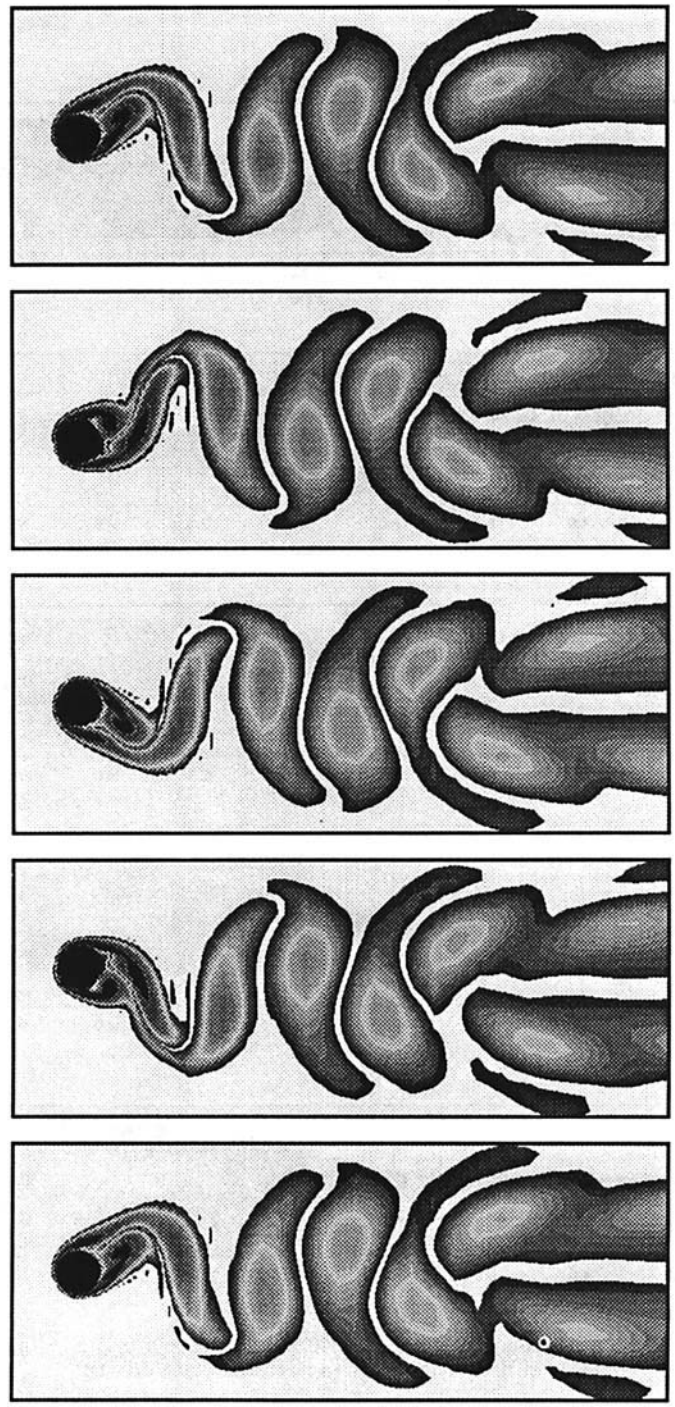

Figure 20. Flow past a vertically oscillating cylinder at $Re = 305$: vorticity at various instants during one period of the cylinder motion

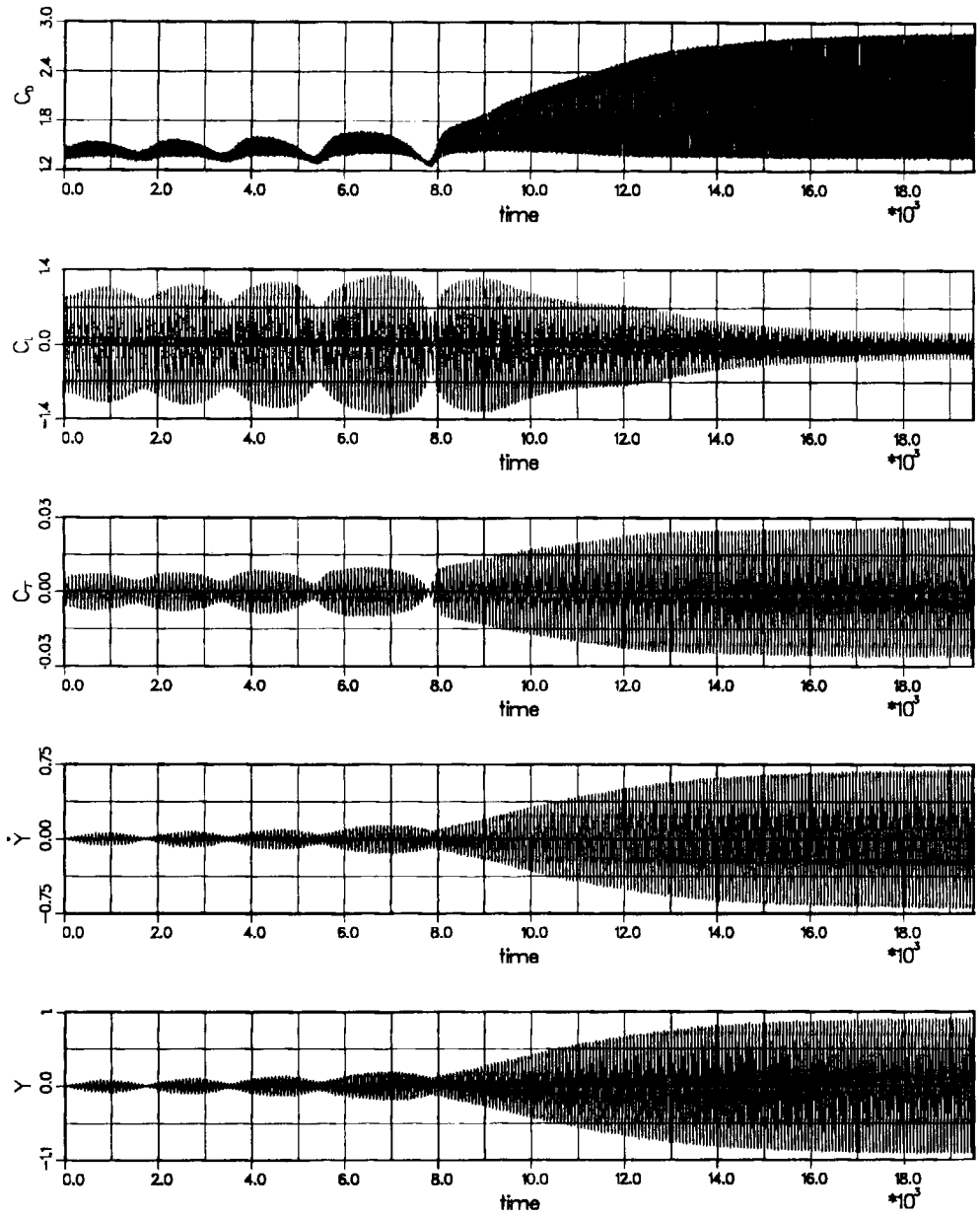

Figure 21. Flow past a vertically oscillating cylinder at $Re = 300$: time histories of the drag, lift and torque coefficients and the normalized velocity and displacement of the cylinder

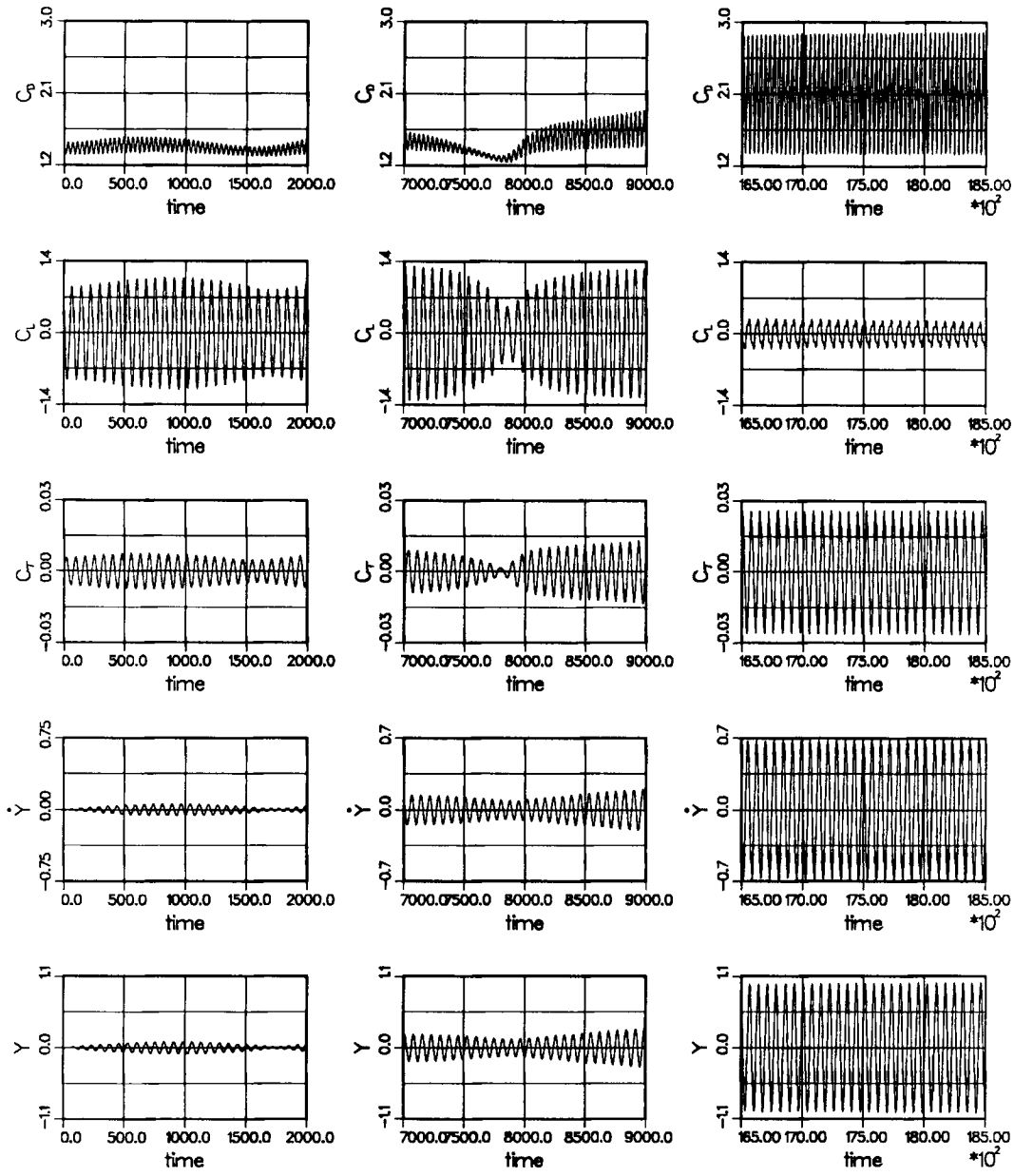

Figure 22. Flow past a vertically oscillating cylinder at $Re = 300$: detailed plots from Figure 21 for three different periods of time

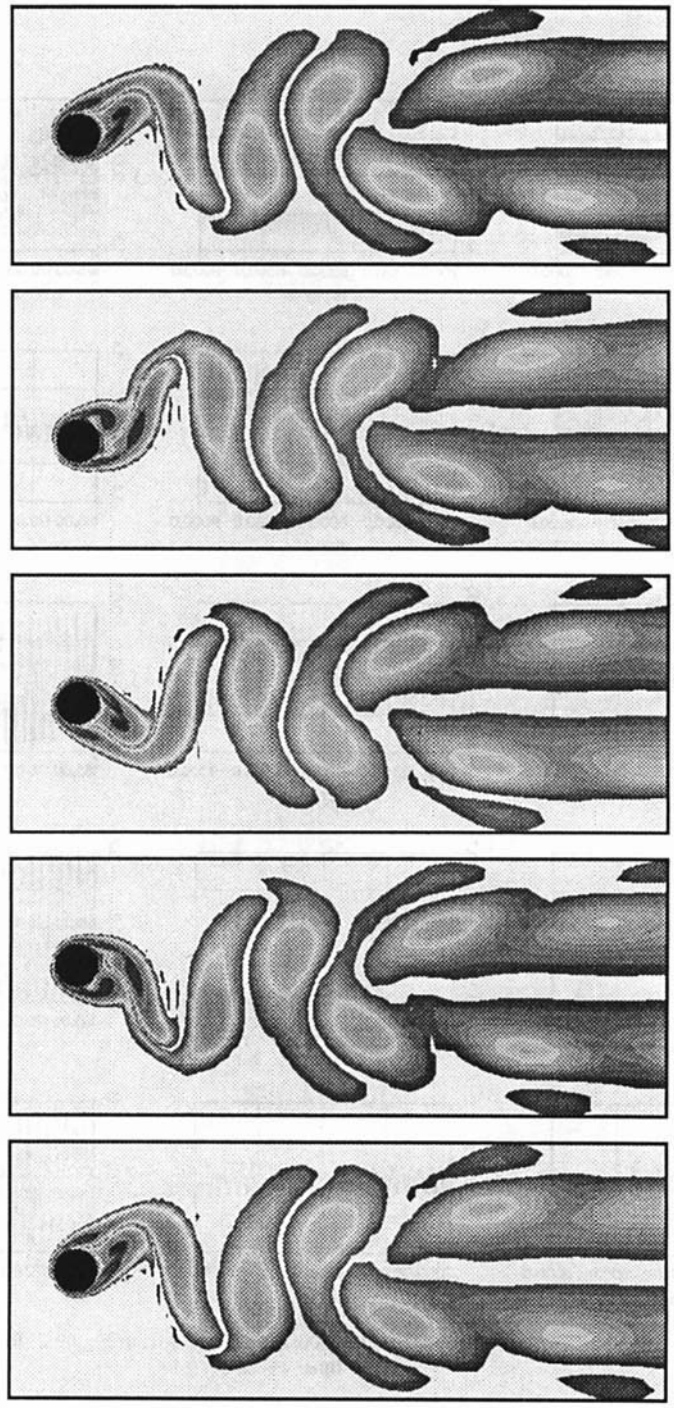

Figure 23. Flow past a vertically oscillating cylinder at $Re = 300$: vorticity at various instants during one period of the cylinder motion

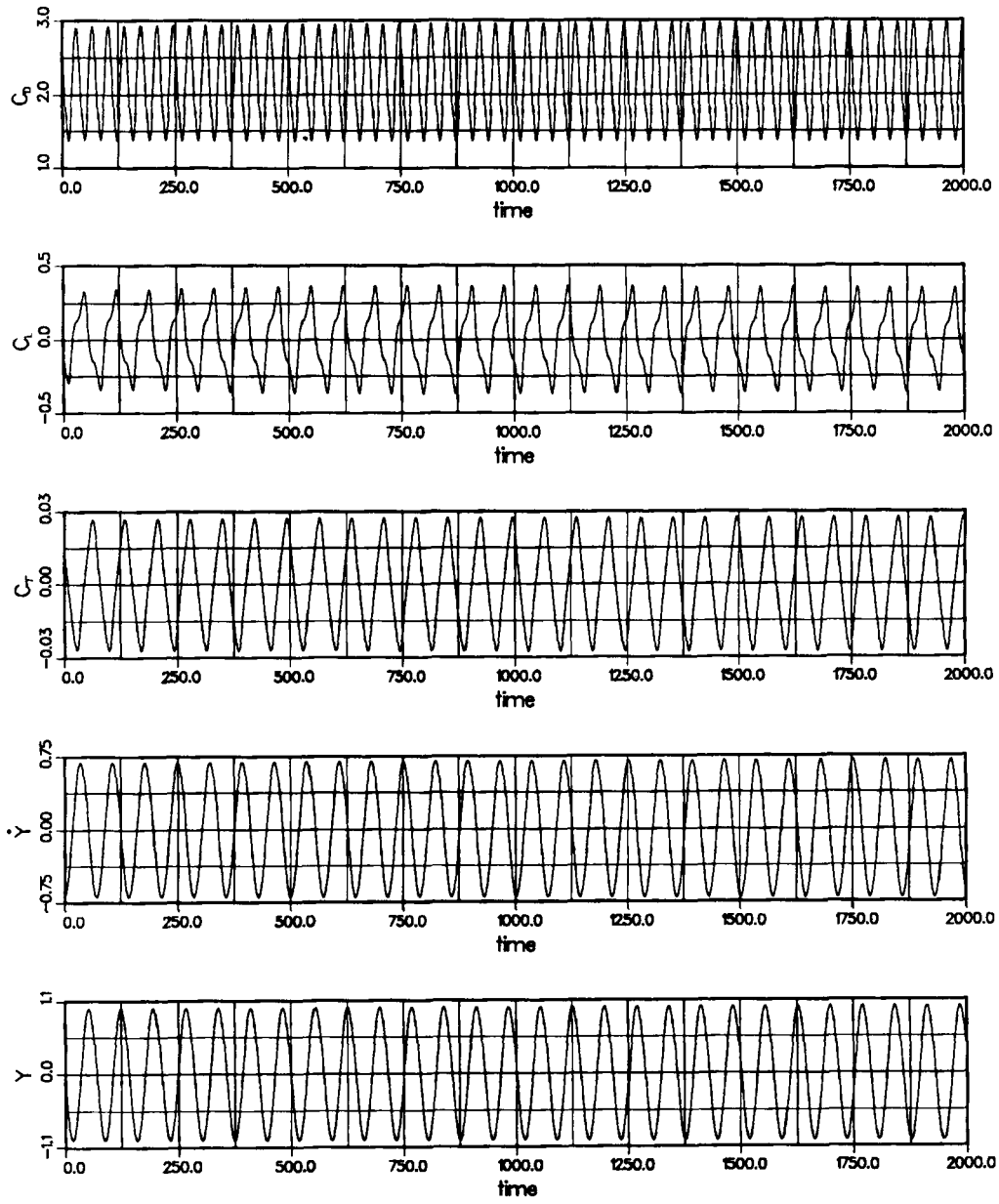

Figure 24. Flow past a vertically oscillating cylinder at $Re = 295$ (high-amplitude solution): time histories of the drag, lift and torque coefficients and the normalized velocity and displacement of the cylinder

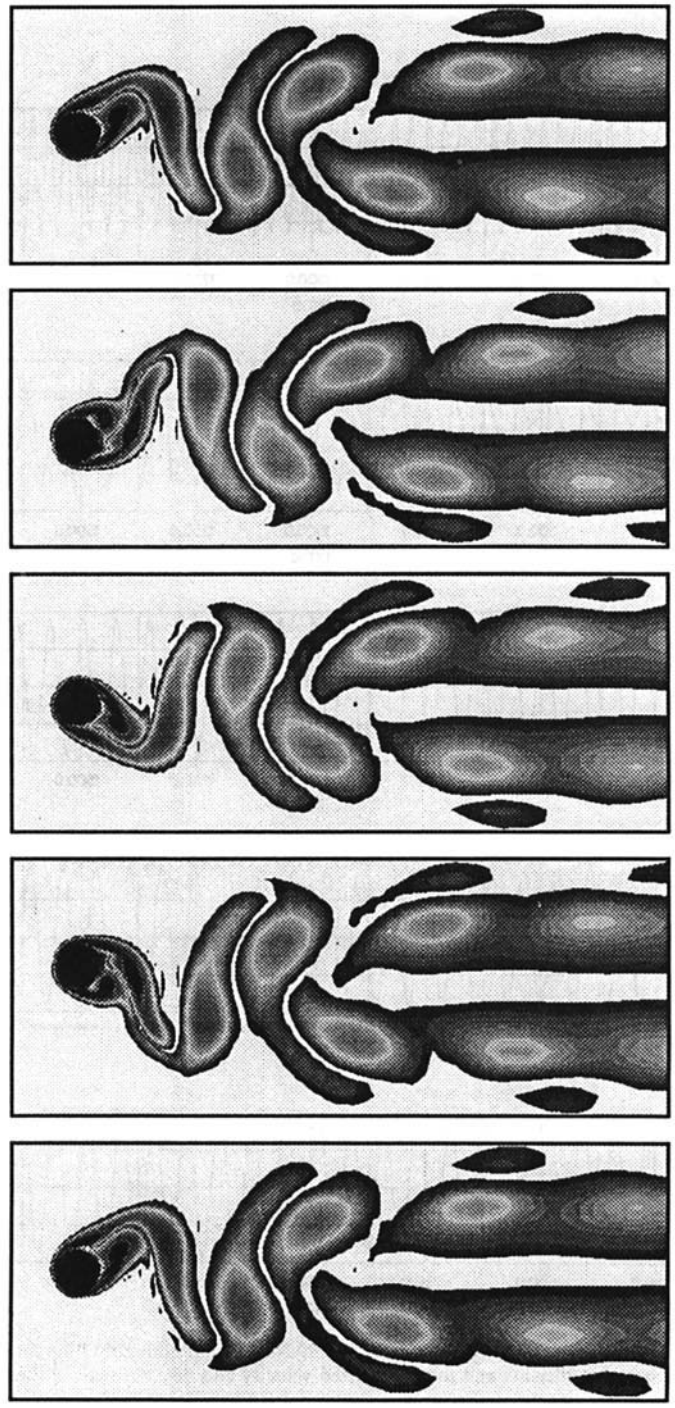

Figure 25. Flow past a vertically oscillating cylinder at $Re = 295$ (high-amplitude solution): vorticity at various instants during one period of the cylinder motion

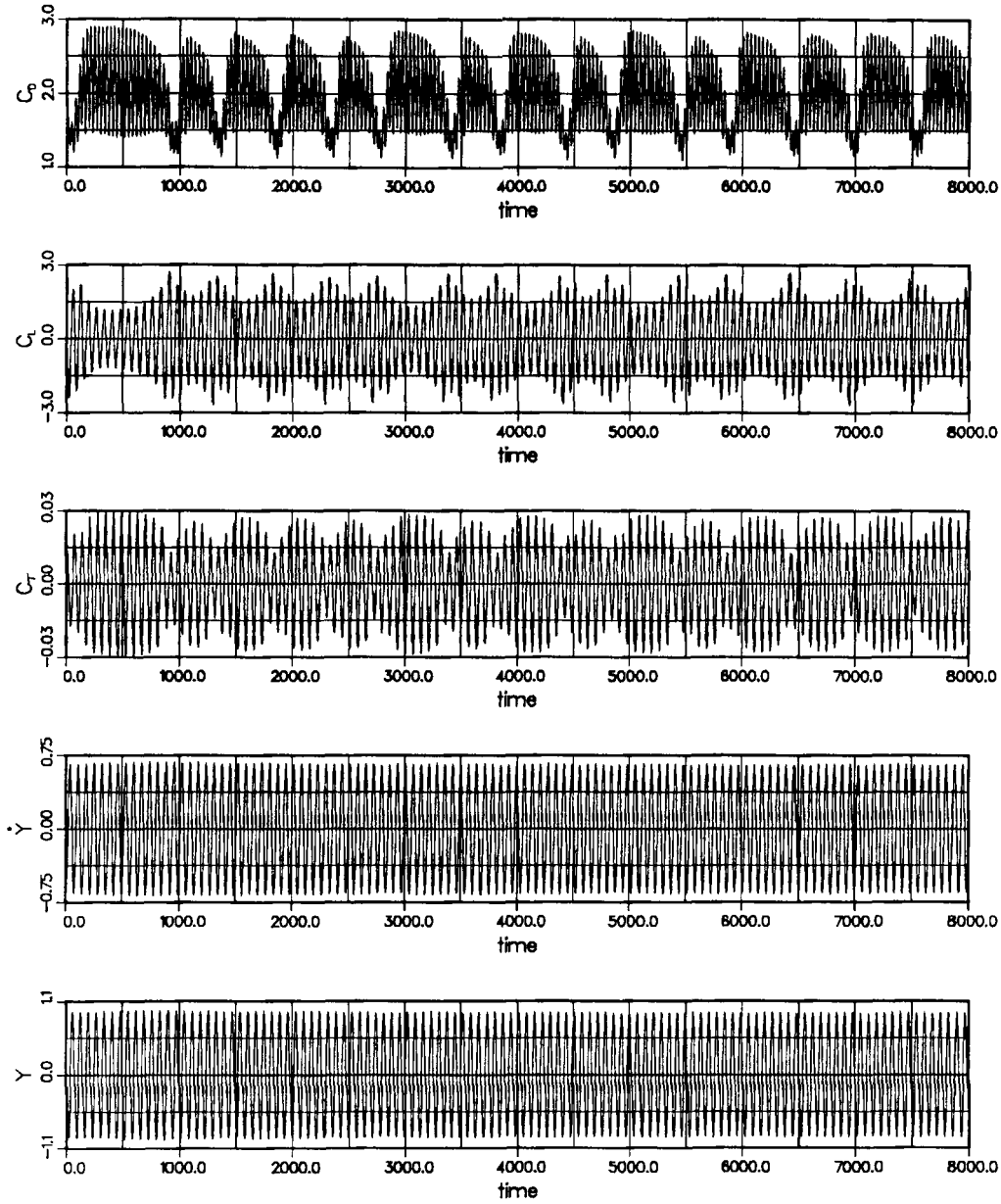

Figure 26. Flow past a vertically oscillating cylinder at $Re = 290$ (high-amplitude solution): time histories of the drag, lift and torque coefficients and the normalized velocity and displacement of the cylinder

displacement and velocity of the cylinder for the high-amplitude solution are shown in Figure 26. Compared to the other cases of high-amplitude solutions, the maximum value of the lift coefficient in this case reaches a very high value. Also, in Figure 26 we observe the presence of more than one temporal frequency in the plots for the drag, lift and torque coefficients. The flow patterns during one period of the cylinder motion in this case are shown in Figure 27. We notice that the disturbance that makes the vortices in the wake unstable and which travels upstream as the Reynolds number decreases now reaches the cylinder. We suspect that this Reynolds number is very close to the end of the lock-in region and below this we may get only one solution—a low-amplitude one. For the low-amplitude solution at Reynolds number 290 the time histories of the drag, lift and torque coefficients and the normalized vertical displacement and velocity of the cylinder are shown in Figure 28.

Variation of lift, torque, drag and cylinder velocity with Reynolds number. Figures 29–31 show the variation of the peak values of the lift, torque and drag coefficients with Reynolds number respectively. From these figures we notice that, compared to the fixed cylinder, the peak value of the drag coefficient for the high-amplitude solution may increase by up to 100% and the lift coefficient may decrease down to less than 25%. We also observe that the minimum value of the drag coefficient is rather insensitive to the amplitude of the cylinder oscillations. The variation of the amplitude of the cylinder velocity (normalized with the freestream velocity) with Reynolds number is shown in Figure 32.

Discussion of multiple solutions. The presence of multiple solutions in the context of vortex-induced oscillations of a cylinder has been reported by other researchers in the past[10] and is referred to as a 'hysteresis'-type behaviour. We are not aware of any work explaining the exact cause of this phenomenon. In the past, researchers have suspected this phenomenon to be a consequence of variable structural damping, a non-linear spring behaviour or a strong non-linearity in the lift coefficient. In this paper we attempt to explain the cause of this double-amplitude behaviour by carrying out a linear oscillator analysis and viewing the resulting cylinder response along with certain experimental data reported by Blevins.[9]

It is well known that the vortex-shedding frequency of an oscillating cylinder can change from the stationary shedding frequency to the vibration frequency of the cylinder if the amplitude of the vibration is large enough. As was pointed out before, this effect is known as 'lock-in'. Figure 33, taken from Reference 9, shows for different vibration frequencies the amplitude of the cylinder vibration needed to cause lock-in. It can be seen that the amplitude of vibration needed to cause lock-in increases with the increase in the ratio of the vibration frequency to the stationary shedding frequency. Also, the shedding frequency of an oscillating cylinder can change by as much as 40% from the shedding frequency for a stationary cylinder.

Let us assume the cylinder to be a linear oscillator, i.e. the motion of the cylinder does not change the flow field; consequently the lift coefficient and the Strouhal number for a fixed and an oscillating cylinder remain the same. Let us also assume that the lift coefficient does not change with the Reynolds number ($C_L = 0{\cdot}9$). Furthermore, let us assume that the shedding frequency of the cylinder follows equation (24). Figure 34 shows the temporally periodic vibration amplitude of the cylinder for various Reynolds numbers with the foregoing assumptions. Also plotted in the same figure is a linear approximation to the curve from Figure 33, the curve that relates the threshold amplitude needed for lock-in to F_n/F_{s0}. We notice that for Reynolds number 324 the linear model predicts a vibration amplitude much larger than what we get from our computations. This is expected because the actual oscillator has a non-linear behaviour and the lift coefficient decreases when the vibration amplitude increases. However, the low-amplitude solutions we get from the non-linear model (i.e. our computations) compare very well with the

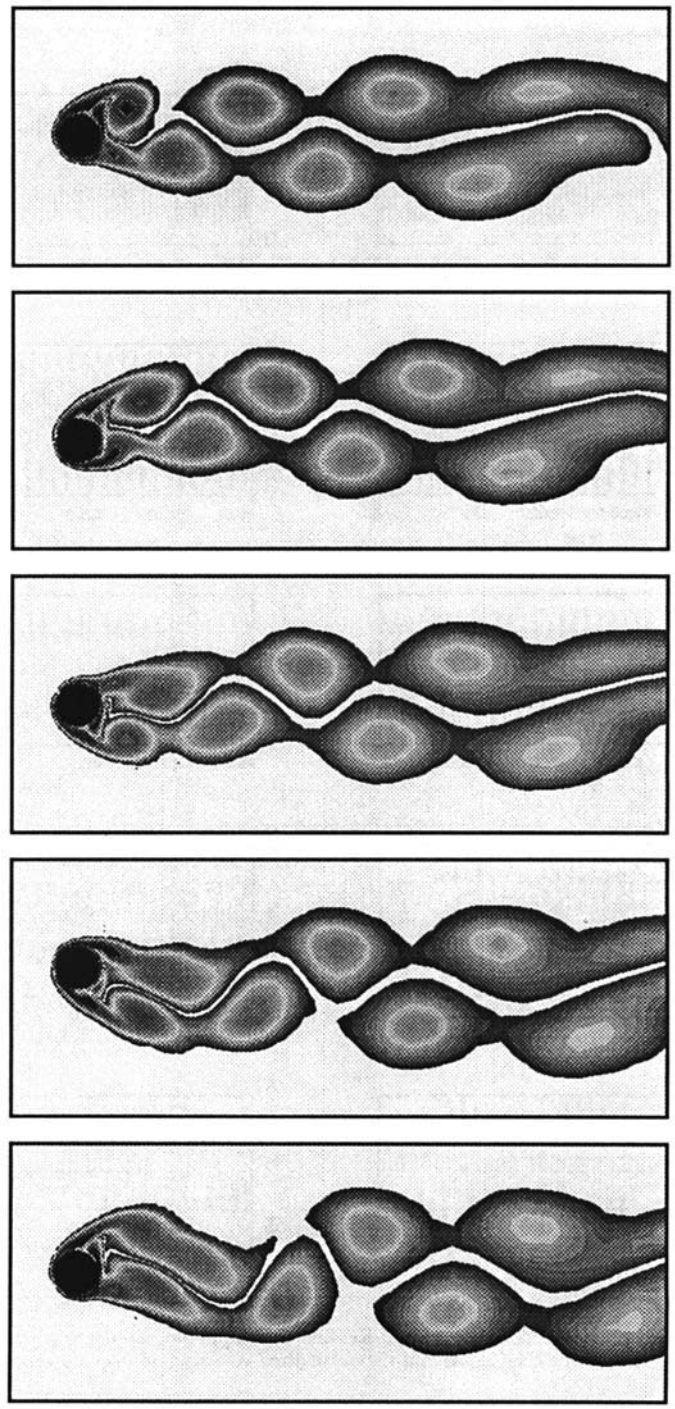

Figure 27. Flow past a vertically oscillating cylinder at $Re = 290$ (high-amplitude solution): vorticity at various instants during one period of the cylinder motion

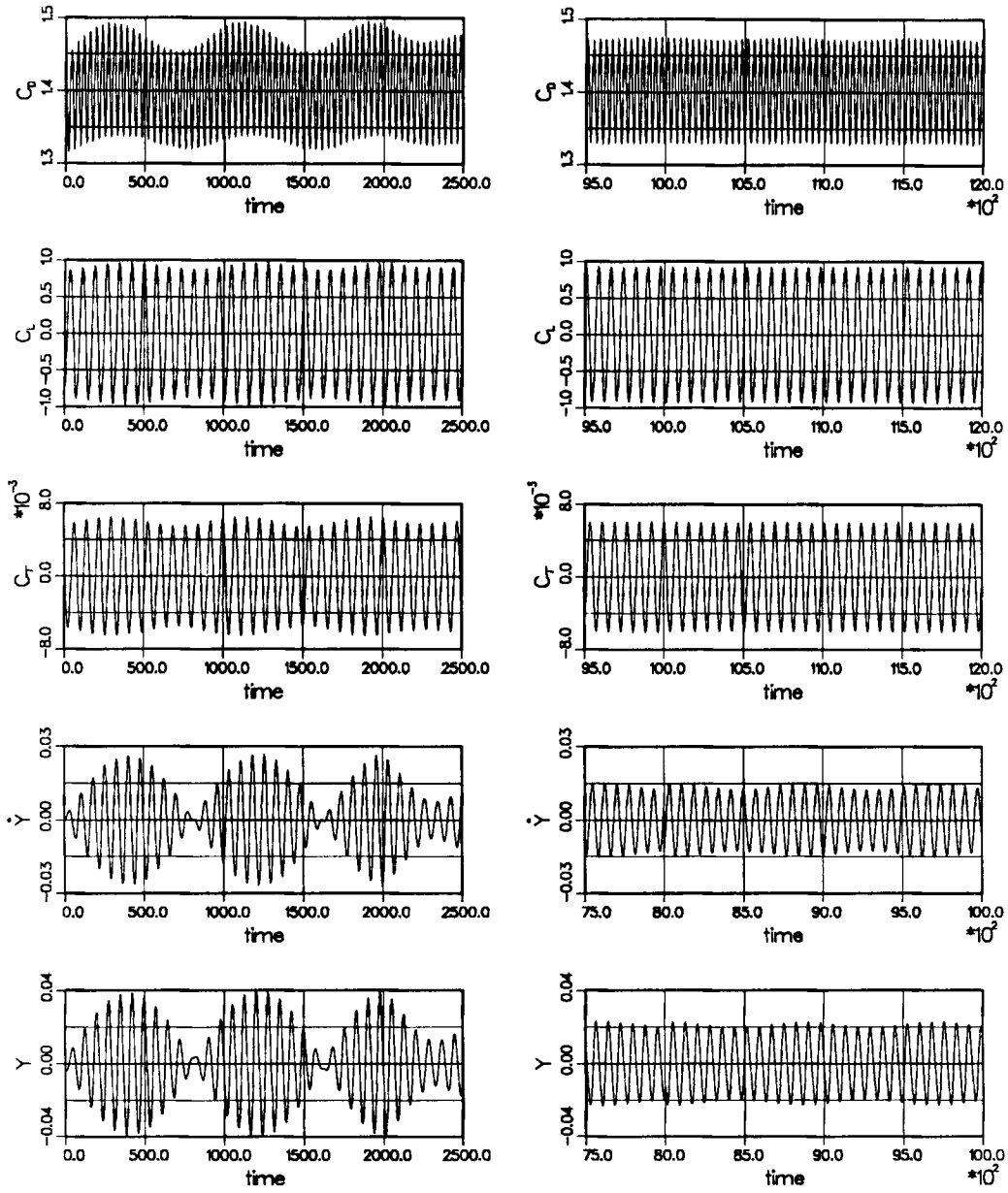

Figure 28. Flow past a vertically oscillating cylinder at $Re = 290$ (low-amplitude solution): initial and later time histories of the drag, lift and torque coefficients and the normalized velocity and displacement of the cylinder

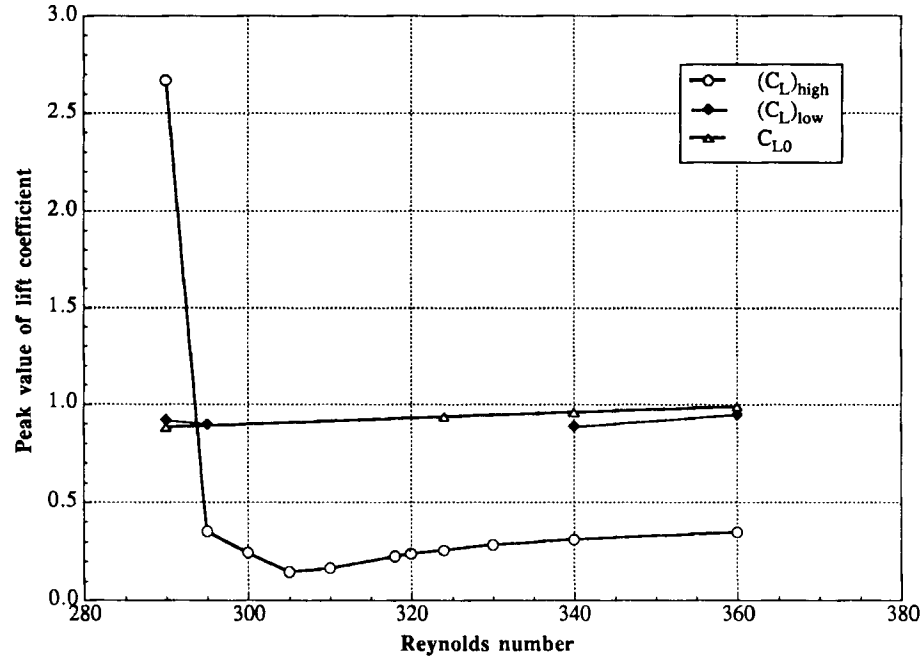

Figure 29. Flow past a vertically oscillating cylinder: peak value of the lift coefficient versus Reynolds number

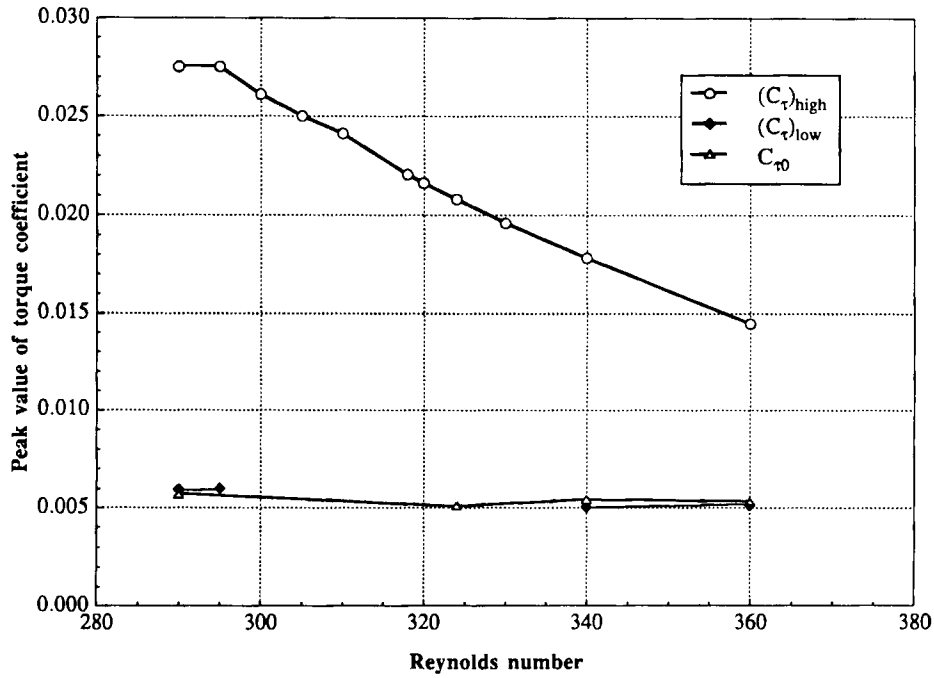

Figure 30. Flow past a vertically oscillating cylinder: peak value of the torque coefficient versus Reynolds number

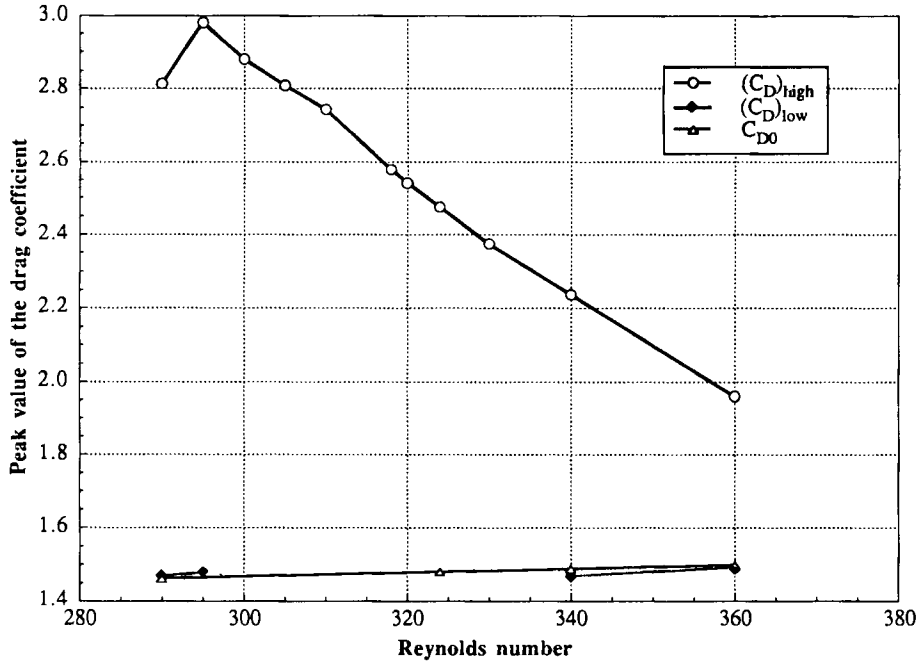

Figure 31. Flow past a vertically oscillating cylinder: peak value of the drag coefficient versus Reynolds number

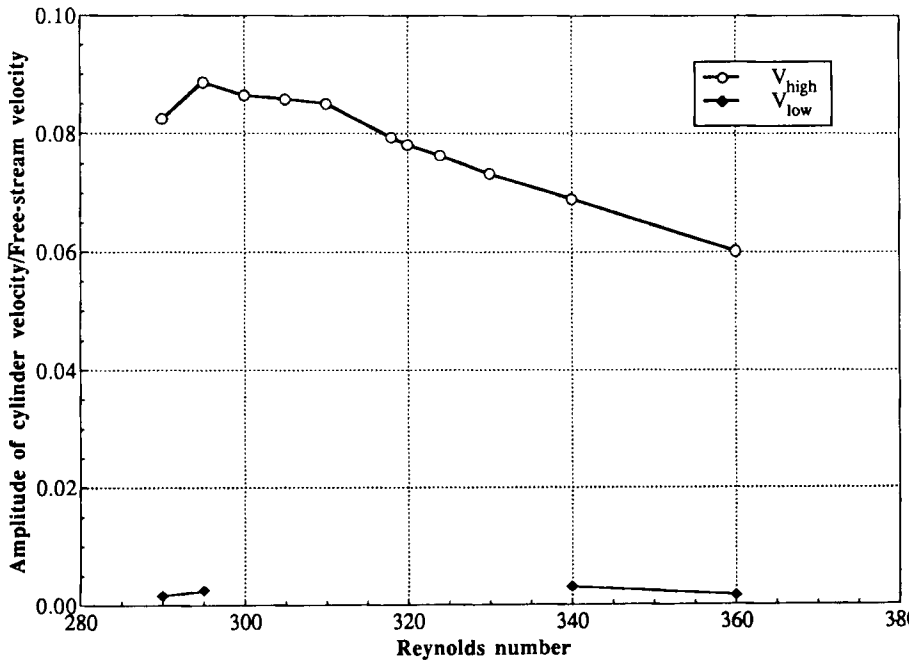

Figure 32. Flow past a vertically oscillating cylinder: non-dimensional velocity amplitude versus Reynolds number

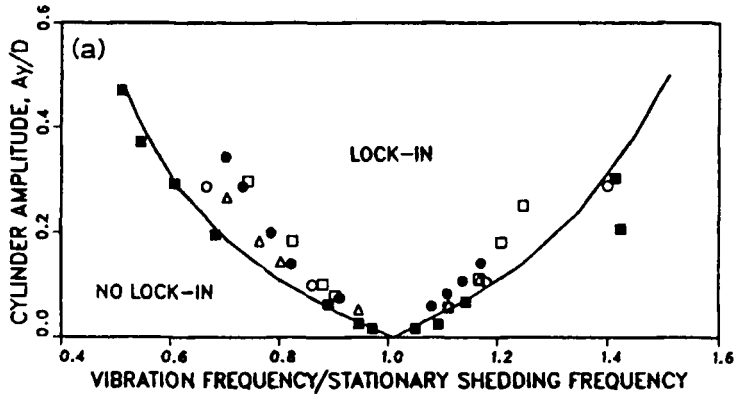

Figure 33. Flow past a vertically oscillating cylinder: lock-in bands for synchronization of vortex shedding with transverse cylinder vibration (photocopied from Reference 9). A_y is the amplitude of transverse vibration and D is the cylinder diameter. Experimental data: Koopmann[12]—□, $Re=100$; ●, $Re=200$; △, $Re=300$; Stansby[16]—■, $Re=3600$; ○, $Re=9200$

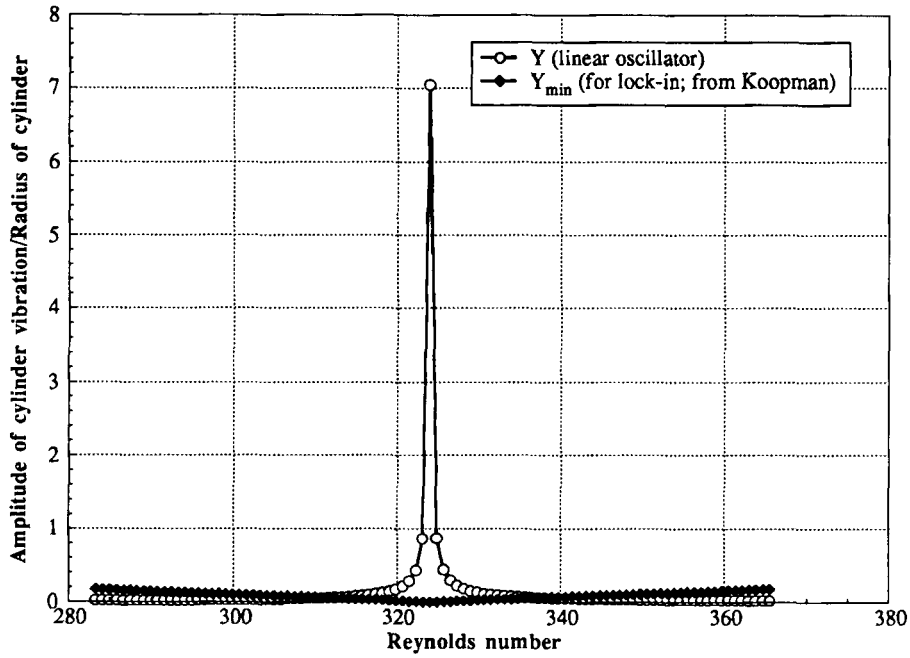

Figure 34. Oscillation amplitude from the linear oscillator model and the minimum value needed for lock-in

vibration amplitudes we get from this linear analysis. Figure 35 shows an enlarged plot from Figure 34 to bring out more clearly the main purpose of this exercise. In Figure 35 the 'V'-shaped region enclosed by the lines from Koopmann's data (extracted from Reference 9) represents the region of lock-in. Consider a flow at Reynolds number 330. The amplitude predicted by the linear oscillator model lies in the lock-in region. Thus, if we release the cylinder from rest, its oscillation amplitude increases, and as soon as it reaches a value of approximately 0·03 cylinder radii, the

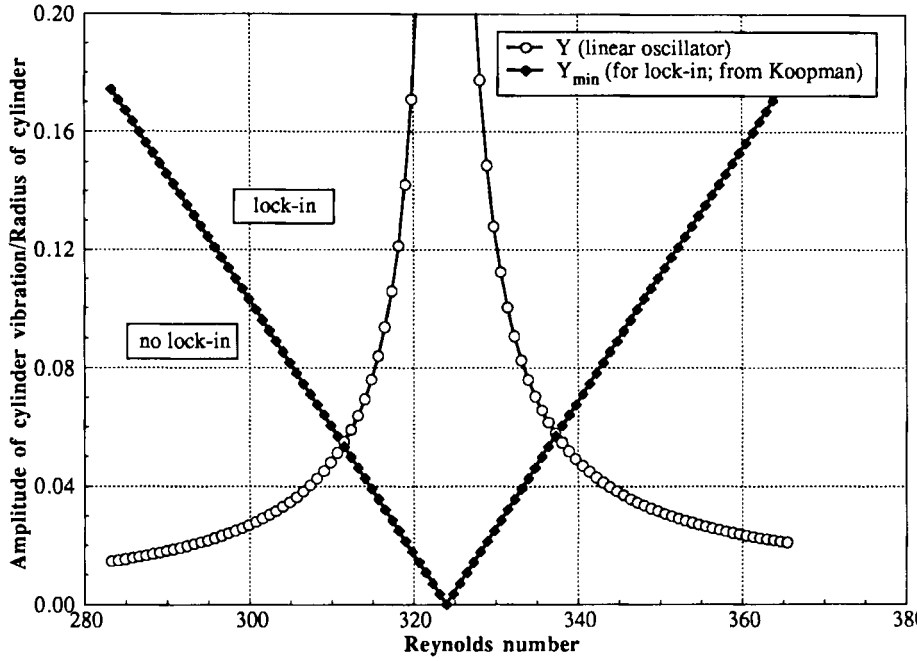

Figure 35. Enlarged plot from Figure 34

shedding frequency locks in to the natural frequency of the spring–mass system and eventually we get a high-amplitude solution. At Reynolds number 360, on the other hand, the amplitude predicted by the linear oscillator model is much smaller than that needed for lock-in. Therefore, when the cylinder is released from rest, it fails to lock in and consequently reaches a low-amplitude solution. However, if the cylinder is initially forced to oscillate with an amplitude higher than that needed for lock-in ($>0{\cdot}155$ cylinder radii), then the shedding frequency locks in to the natural frequency of the spring–mass system. This therefore leads to a high-amplitude solution. The same phenomenon occurs for the range of Reynolds number less than 324. It is interesting to note that for the high-Reynolds-number side our computations yield only one solution at Reynolds number 330 and two solutions for Reynolds number 340; the same prediction can be made from Figure 35. For the low-Reynolds-number side Figure 35 predicts a higher Reynolds number for the beginning of the multiple-solution range than what we get from our computations. This difference can perhaps be attributed to the assumptions we made to linearize the oscillator model and the three-dimensional effects in the experimental data collected by Koopmann (extracted from Reference 9).

4.2. Flow past a pitching aerofoil at Reynolds number 1000

We now present some of our preliminary results for flow past a pitching aerofoil (NACA 0012) at Reynolds number 1000. The Reynolds number is based on the freestream velocity and the chord length of the aerofoil. The dimensions of the computational domain, normalized by the chord length of the aerofoil, are 30·0 and 20·0 in the flow and cross-flow directions respectively. The finite element mesh consists of 6609 nodes and 6460 elements. At every time step, approximately 39 000 equations are solved simultaneously. To solve this equation system, we use the GMRES iteration method with the CEBE preconditioners. The average cluster size is 29 elements

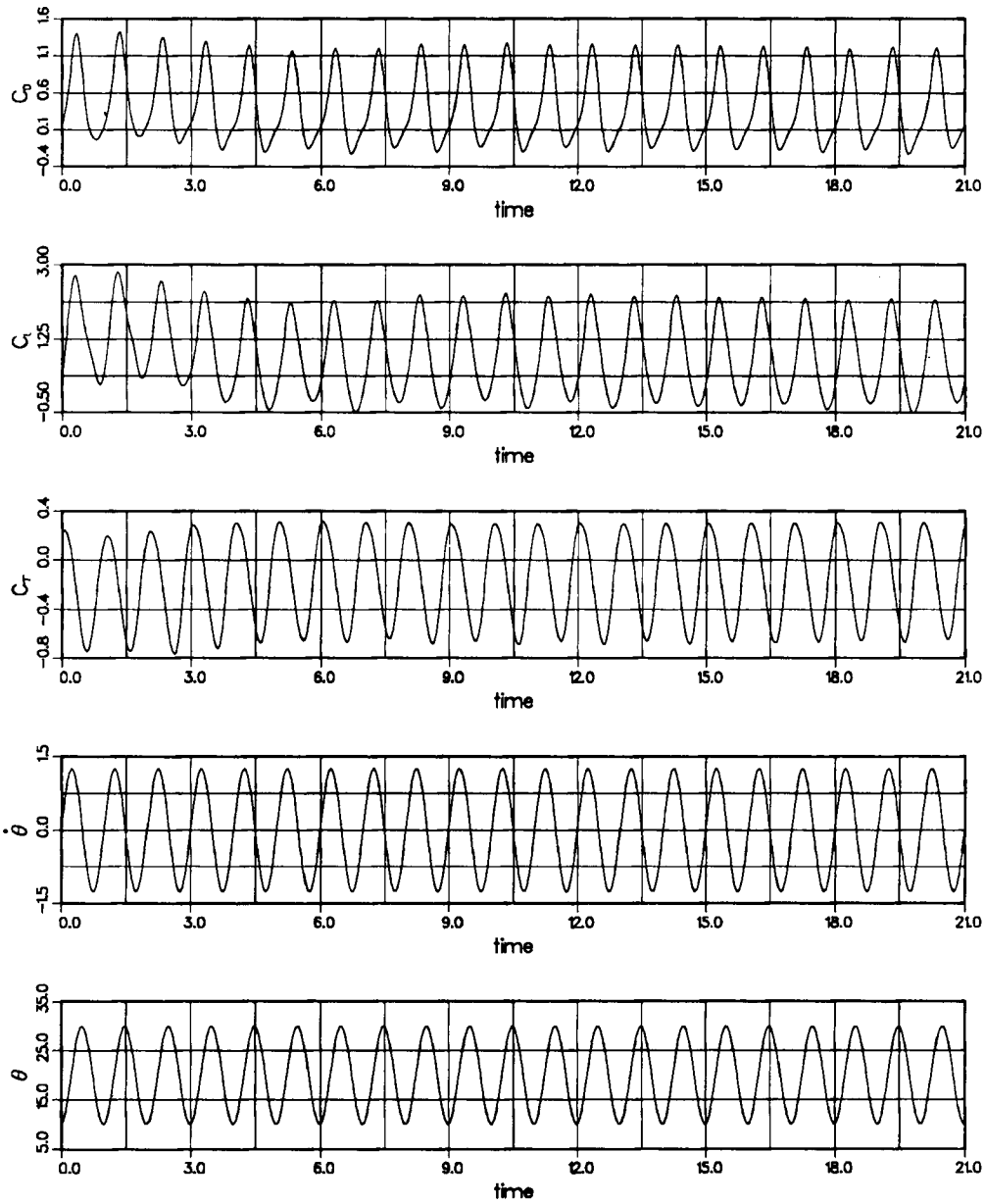

Figure 36. Flow past a pitching aerofoil at $Re = 1000$: time histories of the drag, lift and torque coefficients and the pitching velocity and angle

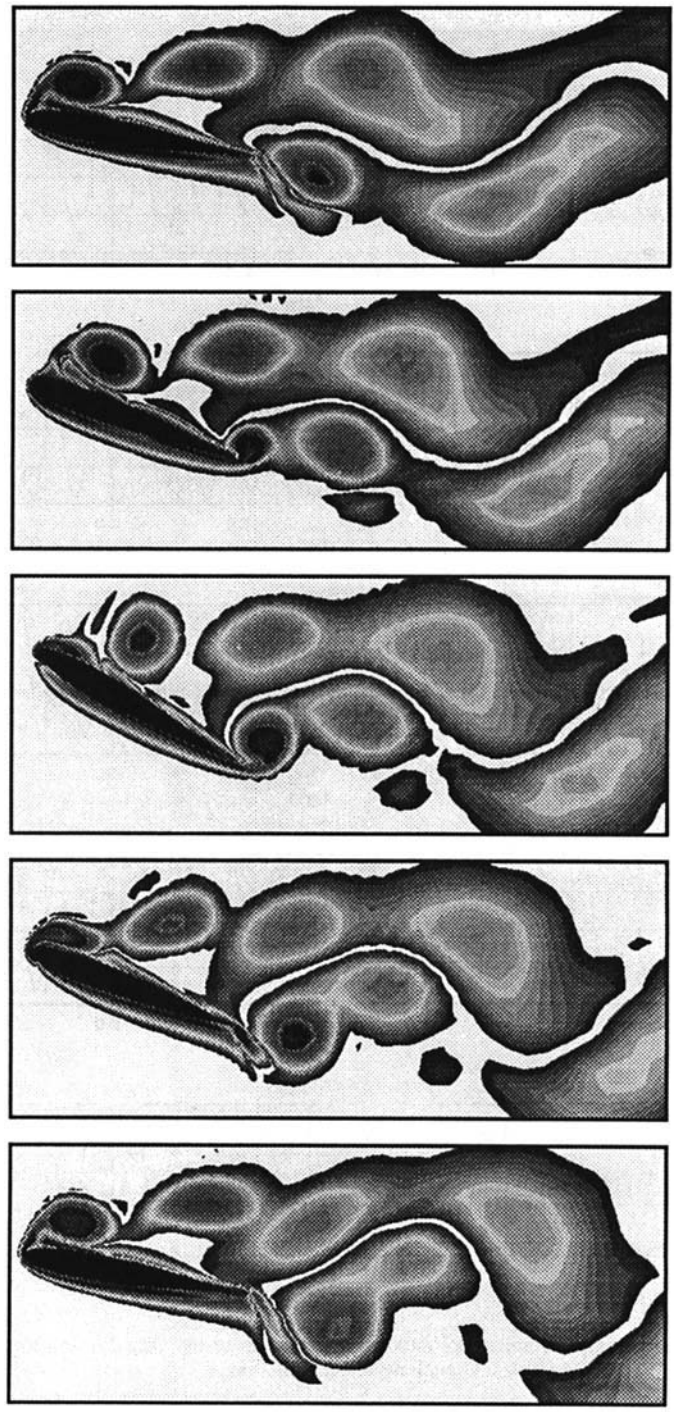

Figure 37. Flow past a pitching aerofoil at $Re = 1000$: vorticity at various instants during one period of the aerofoil motion

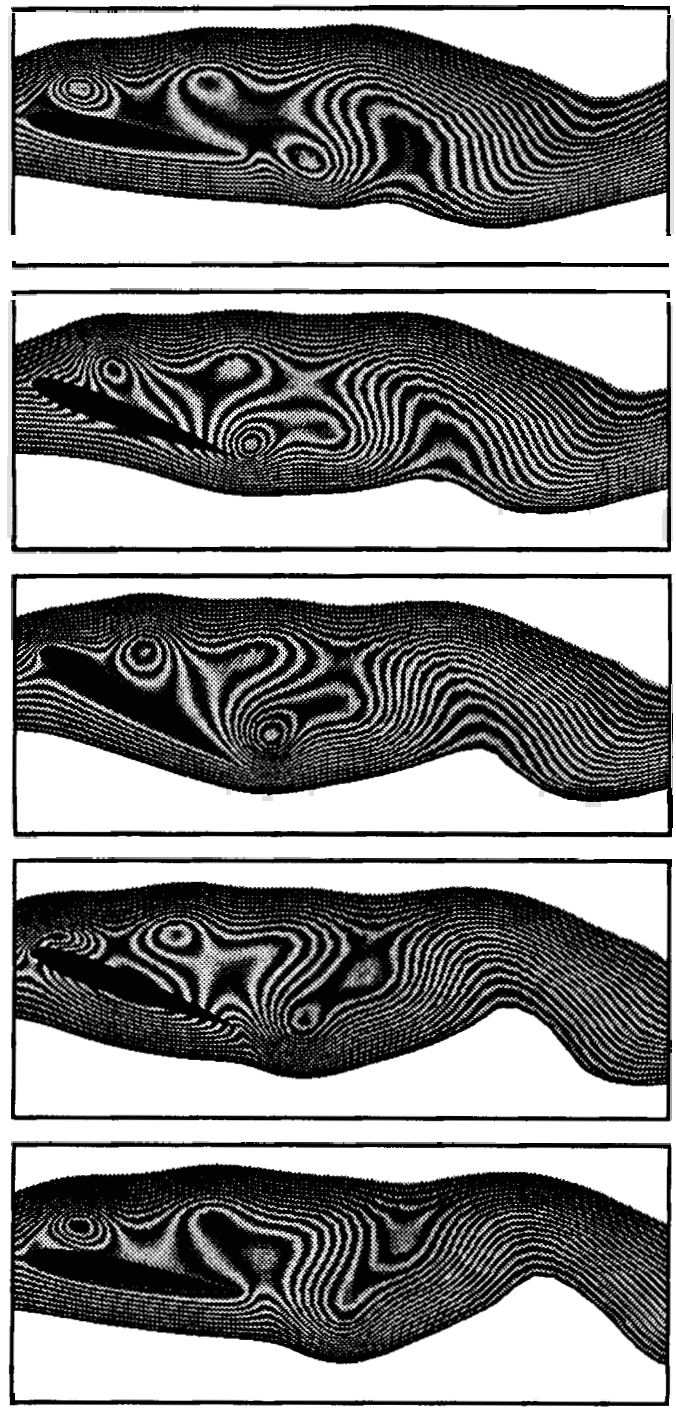

Figure 38. Flow past a pitching aerofoil at $Re = 1000$: streamfunction at various instants during one period of the aerofoil motion

and the dimension of the Krylov vector space is 30. For this problem, compared to the direct solution method, the CEBE technique takes less than one-seventh of the CPU time and approximately one-fourth of the memory. The freestream velocity is 1·0 and the time step size is 0·02. Symmetry conditions are imposed at the upper and lower computational boundaries; the traction-free condition is imposed at the outflow boundary, which is located 20 chord lengths downstream of the half-chord point of the aerofoil. The initial condition is the temporally periodic solution for the flow past a fixed aerofoil at 10° angle of attack. Then the aerofoil is forced to pitch about its half-chord point with the prescribed angular displacement

$$\theta = \frac{\theta_{\max} + \theta_{\min}}{2} - \frac{\theta_{\max} - \theta_{\min}}{2} \cos(\omega_f t), \tag{25}$$

where $\omega_f = 2\pi f_f$. For the present case the value of f_f corresponds to a reduced frequency ($F_f = f_f c / U_\infty$, where c is the chord length of the aerofoil and U_∞ is the freestream velocity) of 1·0. $\theta_{\min}$ and $\theta_{\max}$ are 10° and 30° respectively.

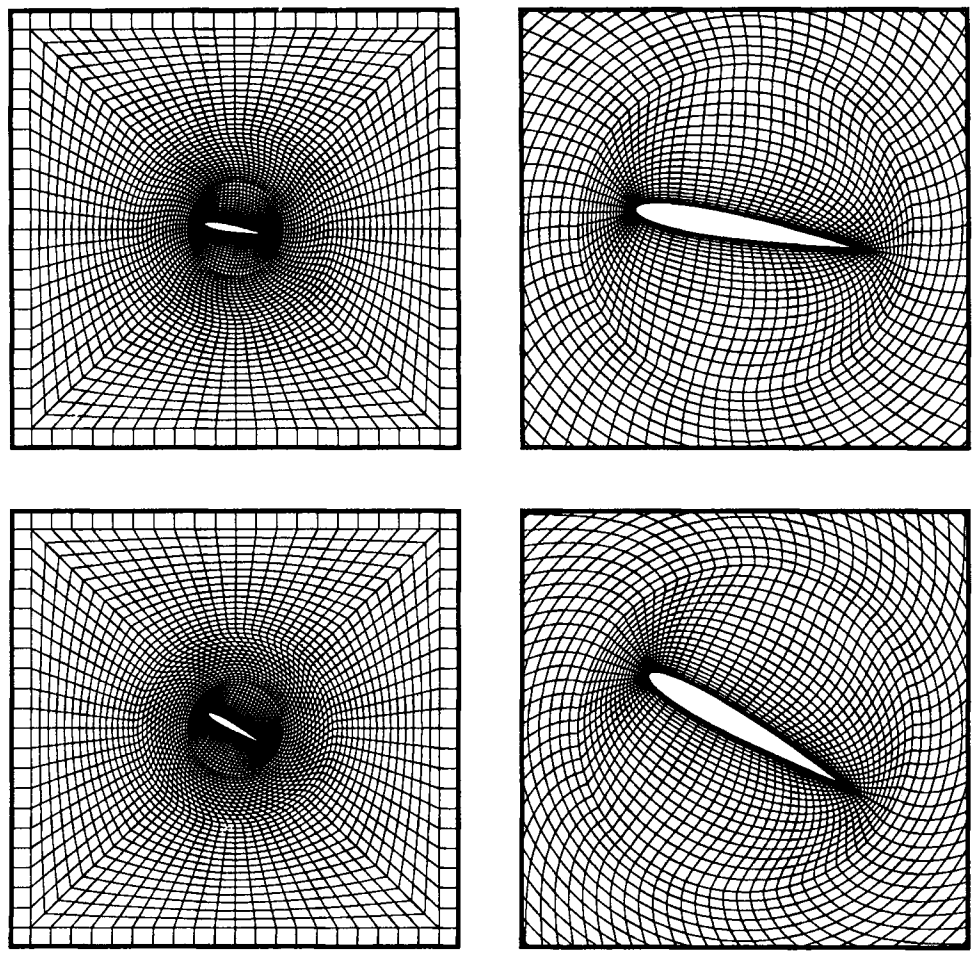

Figure 39. Flow past a pitching aerofoil at $Re = 1000$: finite element meshes corresponding to the two extreme positions of the aerofoil

Figure 36 shows the time histories of the drag, lift and torque coefficients and the angular velocity and displacement (in degrees) of the aerofoil. The drag, lift and torque coefficients oscillate with a dominant non-dimensional frequency of 1·0. Furthermore, the drag coefficient has an additional component at twice the aerofoil pitching frequency. It can also be seen that the peak value of the lift coefficient is much larger than that for a fixed aerofoil. In the context of aeroplane performance, this fact can be exploited by aircraft to attain high lift coefficients by rapid pitching motion during severe manoeuvres. Figures 37 and 38 show a sequence of frames for the vorticity and streamfunction during one period of the aerofoil motion. Qualitatively, these flow patterns compare well with those reported by Tuncer *et al.*[19] and Ohmi *et al.*[20] for a similar (but not the same) aerofoil motion. The finite element meshes corresponding to the two extreme positions of the aerofoil are shown in Figure 39.

5. CONCLUDING REMARKS

The space–time finite element formulation with the Galerkin/least-squares stabilization was used to solve certain unsteady flow problems involving oscillating cylinders and aerofoils. To minimize the computational cost associated with these fairly large-scale problems, the GMRES iteration technique and CEBE preconditioners were employed to solve the implicit equation systems resulting from the space–time finite element discretization. Certain interesting physical phenomena were observed as a result of these computations. Flow past a cylinder subjected to forced horizontal oscillations leads to a symmetric mode of vortex shedding. The case of vortex-excited vertical oscillations was also simulated. The coupling between the fluid flow and the cylinder motion makes the oscillator non-linear and leads to certain interesting phenomena such as 'lock-in' and 'hysteresis'. The cause of the 'hysteresis' type of behaviour of this oscillator was investigated using a linear oscillator model and experimental data reported by other investigators. Preliminary results were presented for flow past a pitching aerofoil at Reynolds number 1000. In all the results presented here, smart mesh-moving techniques were employed to avoid remeshing; consequently, our computations are free from the projection errors associated with frequent remeshing.

ACKNOWLEDGEMENTS

This work was sponsored by the NASA-Johnson Space Center (under grant NAG 9-449), the NSF (under grant CTS-8796352) and the ALCOA Foundation. Partial support for this work has also come from the Army Research Office contract number DAAL03-89-C-0038 with the Army High Performance Computing Research Center at the University of Minnesota.

REFERENCES

1. T. E. Tezduyar, M. Behr and J. Liou, 'A new strategy for finite element computations involving moving boundaries and interfaces– the DSD/ST procedure: I. The concept and the preliminary numerical tests', *Comput. Methods Appl. Mech. Eng.*, **94**, 339–351 (1992).
2. T. E. Tezduyar, M. Behr, S. Mittal and J. Liou, 'A new strategy for finite element computations involving moving boundaries and interfaces—the DSD/ST procedure: II. Computation of free-surface flows, two-liquid flows, and flows with drifting cylinders', *Comput. Methods Appl. Mech. Eng.*, **94**, 353–371 (1992).
3. T. J. R. Hughes, L. P. Franca and M. Mallet, 'A new finite element formulation for computational fluid dynamics: VI. Convergence analysis of the generalized SUPG formulation for linear time-dependent multi-dimensional advective–diffusive systems', *Comput. Methods Appl. Mech. Eng.*, **63**, 97–112 (1987).
4. T. J. R. Hughes and G. M. Hulbert, 'Space–time finite element methods for elastodynamics: formulations and error estimates', *Comput. Methods Appl. Mech. Eng.*, **66**, 339–363 (1988).
5. F. Shakib, 'Finite element analysis of the compressible Euler and Navier–Stokes equations', *Ph.D. Thesis*, Department of Mechanical Engineering, Stanford University, Stanford, CA, 1988.

6. P. Hansbo and A. Szepessy, 'A velocity–pressure streamline diffusion finite element method for the incompressible Navier–Stokes equations', *Comput. Methods Appl. Mech. Eng.*, **84,** 175–192 (1990).
7. Y. Saad and M. H. Schultz, 'A generalized minimal residual algorithm for solving nonsysmmetric linear systems', *SIAM J. Sci. Stat. Comput.*, **7,** 856–869 (1986).
8. J. Liou and T. E. Tezduyar, 'Computation of compressible and incompressible flows with the clustered element-by-element method', *University of Minnesota Supercomputer Institute Research Report UMSI 90/215*, October 1990.
9. R. D. Blevins, *Flow-induced Vibration*, 2nd edn, Van Nostrand Reinhold, New York, 1990.
10. T. Sarpkaya, 'Vortex-induced oscillations', *J. Appl. Mech.*, **46,** 241–258 (1979).
11. R. King, 'A review of vortex shedding research and its application', *Ocean Eng.*, **4,** 141–172 (1977).
12. G. H. Koopmann, 'The vortex wakes of vibrating cylinders at low Reynolds numbers', *J. Fluid Mech.*, **28,** 501–512 (1967).
13. O. M. Griffin and G. H. Koopmann, 'The vortex-excited lift and reaction forces on resonantlv vibrating cylinders', *J. Sound Vibr.*, **54,** 435–448 (1979).
14. W. W. Durgin, P. A. March and P. J. Lefebvre, 'Lower mode response of circular cylinders in cross-flow', *J. Fluids Eng.*, **102,** 183–190 (1980).
15. M. J. Every, R. King and D. S. Weaver, 'Vortex-excited vibrations of cylinders and cables and their suppression', *Ocean Eng.*, **9,** 135–157 (1982).
16. P. K. Stansby, 'The locking-on of vortex shedding due to the cross-stream vibration of circular cylinders in uniform and shear flows', *J. Fluid Mech.*, **74,** 641–665 (1976).
17. K. Edamoto and M. Kawahara, 'Two dimensional finite element analysis for fluid structure interaction problem', *Proc. Fourth Int. Conf. on Computing in Civil and Building Engineering*, The Japan Society of Civil Engineers and The Architectural Institute of Japan, Tokyo, 1991.
18. M. Shimura and O. C. Zienkiewicz, 'Interaction analysis between structure and fluids flow by using the direct Laplacian method', *Proc. Fourth Int. Conf. on Computing in Civil and Building Engineering*, The Japan Society of Civil Engineers and The Architectural Institute of Japan, Tokyo, 1991.
19. I. H. Tuncer, J. C. Wu and C. M. Wang, 'Theoretical and numerical studies of oscilllating airfoils', *AIAA J.*, **28,** 1615–1624 (1990).
20. K. Ohmi, M. Coutanceau, O. Daube and T. P. Loc, 'Further experiments on vortex formation around an oscillating and translating airfoil at large incidences', *J. Fluid Mech.*, **225,** 607–630 (1991).
21. T. E. Tezduyar, S. Mittal, S. E. Ray and R. Shih, 'Incompressible flow computations with stabilized bilinear and linear equal-order-interpolation velocity–pressure elements', *Comput. Methods Appl. Mech. Eng.*, **95,** 221–242 (1992).
22. L. P. Franca and S. L. Frey, 'Stabilized finite element methods: II. The incompressible Navier–Stokes equations', *Preprint*, July 1991.
23. S. Mittal, A. Ratner, D. Hastreiter and T. E. Tezduyar, 'Space–time finite element computation of incompressible flows with emphasis on flows involving oscillating cylinders', *Int. Video J. Eng. Res.*, **1,** 83–96 (1992).